TURUN YLIOPISTON JULKAISUJA
ANNALES UNIVERSITATIS TURKUENSIS

SARJA - SER. A I OSA - TOM. 444

ASTRONOMICA - CHEMICA - PHYSICA - MATHEMATICA

THE LASER QUENCHING TECHNIQUE FOR STUDYING THE MAGNETO-THERMAL INSTABILITY IN HIGH CRITICAL CURRENT DENSITY SUPERCONDUCTING STRANDS FOR ACCELERATOR MAGNETS

by

Eelis Takala

TURUN YLIOPISTO
UNIVERSITY OF TURKU
Turku 2012

From the Wihuri Physical Laboratory
Department of Physics and Astronomy
The Doctoral Programme of the Faculty of Mathematics and Natural Sciences
University of Turku
Turku, Finland
and
The Doctoral Student Program
CERN, Switzerland

Supervised by

Scientific advice	PhD work/advise	PhD plan supervision
Dr. B. Bordini	Prof. L. Rossi	Prof. P. Paturi
Scientist	HL-LHC Project Coordinator	Head of Department
TE-MSC-SCD	TE Deputy Head	Wihuri Physical Laboratory
CERN	CERN	Dept. of Physics and Astronomy
Geneva	Geneva	University of Turku
Switzerland	Switzerland	Turku, Finland

Reviewed by

Prof. A. Mailfert
Laboratoire Environnement Minéralurgie
Ecole National Supérieur de Géologie
ENSG Bat. A
Rue du Doyen Marcel Roubault
54500 Vandoeuvre les Nancy, France

Dr. Giovanni Volpini
Istituto Nazionale di Fisica Nucleare
Laboratorio Acceleratori e
Superconduttività Applicata
via f.lli Cervi 201
20090 Segrate(MI), Italy

Opponent

Dr. A. Devred
Section Leader
Superconductor Systems and Auxiliaries Section
ITER Organization, Building 507/021, TKM, Magnet Division
Route de Vinon sur Verdon - 13115 St Paul Lez Durance, France

ISBN 978-951-29-5128-4 (PRINT)
ISBN 978-951-29-5129-1 (PDF)
ISSN 0082-7002
Painosalama Oy - Turku, Finland 2012

Abstract

The energy and luminosity upgrades of the LHC are calling for a strong development of high performance superconducting strands. It is important to know the limitations of the superconductor. One of the remaining issues is the *Magneto-Thermal Instability* (MTI), which can be a severe drawback in high J_c superconducting strands. The basic theory of the phenomenon is well understood. The MTI is initiated by a perturbation, which is a small trigger energy that can be considerably lower than the minimum quench energy. The theoretical and experimental results suggest that the quench current is strongly dependent on the external perturbation. The hypothesis of the theory can't be put into a rigorous test without being able to control the trigger energy responsible for the initiated instability. The original part of this work is the use of so called *Laser Quenching Technique* (LQT) and its further development for particularly studying the perturbation sensitivity of the MTI in the high J_c superconducting strands for which the existing methods are not applicable. They are too slow or suffer from fundamental energy efficiency problems. The LQT apparatus relies on the Q-switched laser technology, providing pulse widths in the nano second time scale which are much shorter than the thermal time constant of the copper stabilizer. The apparatus is optimized with respect to the wavelength in order to have the highest possible energy efficiency for depositing the trigger energy. The LQT pulse is guided by an all-silica fibre. Work is done to understand how well the fibre adapts to the cryogenic temperatures and what is the wavelength for having the highest possible absorptivity in the copper surface of the strand without inducing irradiation damage in the fibre. The system is calibrated at 4.2 K to determine the cryogenic optical loss and the optical absorptivity of the copper. The LQT is used to deeply test the theory of MTI and to provide more information to magnet technology. One of the most important strands, a 0.7 mm RRP 108/127 has been fully characterized with the LQT: the experiment confirmed the predictions of the theory about the perturbation sensitivity. Moreover, filament cut technique for improving the self-field stability of superconducting strands is presented. The technique is based on cutting the outermost superconducting sub-elements of the strand in the splice region without changing the nominal current capacity. The technique forces the current in the innermost filament layers and thus provides a so called self-field barrier at the outermost filament layer, which is a stable region in a superconductor between the external perturbation and the transport current. Similar barrier is also generated in a conventional strand by a special ramp up scheme and the LQT is used to verify the increased stability.

Preface

After finishing my masters degree at the University of Turku in Autumn 2007, I worked at the Magnet Technology Center (MTC) of Prizztech Ltd. in Pori for a bit over one year. I worked under the supervision of Dr. Martti Paju. During this time I learnt valuable lessons in the field of Magnet Technology as well as applying my academic training in real work. I also had time to think over my academic future. Without this experience and new contacts I probably would have never applied to the Doctoral Student Program at CERN. I sent my application after visiting the place in Spring 2008.

During my stay at Pori I became good friends with Dr. Pekka Suominen who is a very skilled physicist. He had been working at CERN just before we met and his encouragements and stories made me revive my only and very valuable CERN contact at the time. I first learnt about CERN from my father's (Dr. Mikko Takala) friend Dr. Markus Nordberg in the first year of my master's degree in 2004. Markus is the Resources Coordinator of the ATLAS Experiment at CERN. Another very important contact for me was Antti Heikkila who works as part of the Big Science Activation Team at CERN. I met him thanks to the contact network of MTC and especially thanks to Pekka who knew Antti very well. Antti Heikkila was a very important person to know: he was so kind to read my CV and make the contact between me and Prof. Lucio Rossi who later on selected me as his PhD student. Moreover, he offered my wife a job while we lived in the Geneva area during years from 2009 to 2012.

During my visit at CERN with my wife, I arranged a meeting with Antti Heikkila and Markus Nordberg and another meeting with Lucio Rossi. The first one was a casual lunch, where the two gentlemen explained to me how the world at CERN functions. This was really helpful to my application for the PhD student program. I have one question though, who paid for the lunch at CERN? Antti and Markus, after you have read this, please tell me who paid. The second meeting was supposed to be with Lucio Rossi, however as he was very busy, he arranged an interview for me with one of his colleagues. We were also in a very nice tour of CERN organized by Lucio Rossi. After the visit, I sent the PhD student application to CERN right away. Later, in Autumn 2008 I was selected.

In January 2009 I started working at CERN under the supervision of Lucio Rossi. At the time, he was the group leader of the *magnets, superconductors and cryostats group* in the *technology department* (TE-MSC). I was placed in one of its sections called

superconductors and devices (TE-MSC-SCD). Lucio Rossi is one of a kind. A strong character who does not have unfinished businesses idling. I was very lucky to have such powerful backup and supervision: no matter how big or small my problems were, he reacted on them immediately. I think he is the only person who *always* answers to my emails and usually even within a few hours which has to be very rare for a man in his position.

Lucio Rossi provided me with the best there is in terms of assistance, co-operation and materials for completing my work. Right in the beginning I started working with Dr. Bernardo Bordini, who later on became my day to day supervisor, a very intelligent and respected author in the field of magneto-thermal instability in accelerator magnets. He taught me almost everything that I know about stability. He was fair and generous, always listened to my ideas, even if he was very busy. It was my task to provide hard evidence on his theory about the self-field instability in Nb_3Sn strands. Among other little projects we started off with an ambitious plan to model the strands in 3D. The models worked remarkably well, but they were too slow and laborious to work with. In parallel we did conventional critical current and stability measurements on the strands.

My favorite experiment of all was based on Dr. Bordini's idea to force the current inside the strand in order to increase the stability. This experiment was later known as the cutting filament effect [**P5**]. The experiment was initiated by Bordini during the first year of my work at CERN. This experiment was the one that made me very excited of self-field instability as it provided a concrete example of the theory.

I dedicated my second year to designing my own experiment for triggering the instabilities. Lucio Rossi gave me the idea to use an existing method (LQT) that Dr. Frederic Trillaud developed for his PhD experiments on the thermal stability of NbTi strands. This seemed like an excellent idea since every other method was too slow or fundamentally problematic. I got in contact with Frederic Trillaud who guided me in the right direction in the beginning. Even the system that Trillaud used was not fast enough. I also encountered some other problems resulting into me having to design my LQT system that was completely a new arrangement with Q-Switching technology and UV-enhanced fibres.

The LQT system development brought new contacts about. I met Prof. Karl-Friedrich Klein who is one of the leading authors in the field of UV enhanced fibre optics. He was the most important external contact in my project. He is a hard working professor from the University of Applied Sciences Friedberg-Giessen who always did what he promised. Without his help, the project would not have been finished. He taught me

a lot and provided me with resources for our collaborative experiments, helped me to solve problems with the laser system and I even had the change to visit his laboratory in Friedberg. His son Mr. Felix Klein and associate Mr. Rene Wandschneider helped me to conduct the critical and fruitful experiment on the optical fibres [**P1**]. Without this work, we would not have the confidence that we posses in our LQT system.

The LQT system development suffered the usual problems of projects in big organizations: a lot of planning and arrangements before anything can happen. Moreover, it took time to make the laser work properly. In July 2011, after careful testing, planning and arranging we managed to calibrate the LQT system in cryogenic temperatures. This project was done with the help of Dr. Johan Bremer who was the leader of *cryogenics laboratory and instrumentation section*. He is a very helpful and efficient man, it was a pleasure to work with him and his subordinates. Moreover Dr. Luca Bottura who was the leader of my section had a supervisory role in designing the experiment, provided resources and made contacts with the right people. He is an extremely intelligent and reasonable authority. He is also the calmest Italian that I ever met. The publication [**P3**] is the statement of this story. I think it is not possible to give the full credit that this publication deserves without knowing how much work was done behind the scenes. Only those who saw what had to be done for it, understand. The development of this LQT system was the most laborious part of my PhD.

I had roughly three months before the end of my contract to do measurements with the new LQT system. I decided to dedicate the time for one sample and try to get everything out of it. In the end I used two weeks for measuring the sample. It paid off because not only was I able to provide hard evidence on the self-field instability but I found the self-field barrier which supported the theory that was behind the beloved cutting filament effect. Well, in the end I had time to measure other samples, too.

From the very first days at CERN, I made a very good friend who is also a colleague of mine, Michiel de Rapper. He was working in the same office as me, doing his PhD like me, concentrating on the thermal stability of the Nb_3Sn cables. We helped each other at work and we had a good time outside the office with our wives who became good friends as well. During our stay at CERN me and my wife met interesting people and found a very nice church community. We miss many things from the area that gave us unforgettable memories and the possibility to interact in an international environment.

This thesis is based on the work that was carried out at CERN during the years from 2009 to 2012. The thesis was written during the following 8 months with the financial support of University of Turku foundation. During all these years, Prof. Petriina Paturi

has given her support to my PhD work. She is an extremely efficient and active person who helped me to succeed and complete all aspects of my PhD work. Moreover she helped with the proof reading of the thesis and with several publications.

The thesis consists of the introductory part and the following publications:

[**P1**] E. Takala, K. F. Klein, B. Bordini, L. Bottura, J. Bremer, L. Rossi, *Silica-Silica Polyimide Buffered Optical Fibre Irradiation and Strength Experiment at Cryogenic Temperatures for 355 nm Pulsed Lasers*, Cryogenics, **52(1)** (2012) 77

[**P2**] J. C. Heimann, C. P. Gonschior, K.-F. Klein, G. Hillrichs, E. Takala, *Spectral UV-losses in 355 nm pulsed laser delivery system at low temperatures*, J. N.-Crys. Solids, **submitted** (2012)

[**P3**] E. Takala, B. Bordini, J. Bremer, C. Balle, L. Bottura, L. Rossi, *An Experimental Setup to Measure the Minimum Trigger Energy for Magneto-Thermal Instability in Nb_3Sn Strands*, IEEE Trans. Appl. Supercond., **22(3)** (2012) 6000704

[**P4**] E. Takala, B. Bordini, L. Rossi, *Perturbation Sensitivity of the Magneto-Thermal Instability*, IEEE Trans. Appl. Supercond., **accepted** (2012), DOI: 10.1109/TASC.2012.2217492

[**P5**] E. Takala, B. Bordini, L. Rossi, *Improving Magneto-Thermal Stability in High J_c Nb_3Sn Superconducting Strands via Filament Cut Technique* , IEEE Trans. Appl. Supercond., **accepted** (2012)

[**P6**] B. Bordini, M. Bajko, S. Caspi, D. Dietderich, H. Felice, P. Ferracin, L. Rossi, G. L. Sabbi, E. Takala, *Magneto-Thermal Stability in LARP Nb_3Sn TQS Magnets*, IEEE Trans. Appl. Supercond., **20(3)** (2010) 274

[**P7**] W. M. de Rapper, L. R. Oberli, B. Bordini, E. Takala, H. H. J. Ten Kate, *Critical Current and Stability of High-J_c Nb_3Sn Rutherford Cables for Accelerator Magnets*, IEEE Trans. Appl. Supercond., **21(3)** (2011) 2359

[**P8**] B. Bordini, L. Bottura, L. Oberli, L. Rossi, E. Takala, *Impact of the Residual Resistivity Ratio on the Stability of Nb_3Sn Magnets*, IEEE Trans. Appl. Supercond., **22(3)** (2012) 4705804

My contributions to the papers is given below:

[**P1**]: I organized the collaborative experiment conducted by CERN and University of Applied Sciences Giessen-Friedberg. I was in charge of the experiments supervised by Prof. Karl-Friedrich Klein. I took part in all the testing and preparations together with Felix Klein, Rene Wandschneider and the staff from Cryolab at CERN. I analyzed the results under supervision of Prof. Klein and I wrote the publication under supervision of Prof. Klein, Prof Rossi and Dr. Bordini.

[**P2**]: My scientific contribution in [**P1**] lead to hypothesis that was discovered during the analysis. The hypothesis was tested in [**P2**] .

[**P3**]: I organized the experiment and took part in all the preparations and I conducted all the measurements. I analyzed the results under supervision of Dr. Bordini. I wrote the article under supervision of Prof. Rossi and Dr. Bordini.

[**P4**]: I organized the experiment and took part in all the preparations and I conducted all the measurements. I analyzed the results under supervision of Dr. Bordini. I wrote the article under supervision of Prof. Rossi and Dr. Bordini. I came up with the concept of self-field barrier.

[**P5**]: I conducted the measurements and sample preparations. I took part in developing the right cutting method together with Dr. Scheuerlein and Dr. Bordini. I analyzed the results under supervision of Dr. Bordini and I wrote the article under supervision of Prof. Rossi and Dr. Bordini.

[**P6**]: I conducted the full critical current and stability characterization of the short sample with and without the Stycast glue. I analyzed the short sample results under supervision of Dr. Bordini.

[**P7**]: I conducted the full characterization of the short sample at 1.9 K and 4.3 K which was compared to the cable results.

[**P8**]: I conducted the preparations and the heat treatments of all the five samples. I conducted the full characterization of the samples at 1.9 K and 4.3 K.

Acknowledgments

I am grateful for this *once in a life time* opportunity. I hope the reader will take a few minutes to go through the preface of this book which gives a better understanding of the appreciation that I have for all the people that have helped me.

This work was financially supported by the *Doctoral Student Program* of CERN during the years from 2009 to 2012. The experiments were conducted at CERN under the *technology department* (TE-MSC-SCD). The writing of the thesis during 8 months in 2012 was supported by the University of Turku foundation.

My supervisors, Dr. Bernardo Bordini, Prof. Lucio Rossi and Prof. Petriina Paturi, you have provided me with the greatest scientific framework to reach my goal. You are the cornerstones on which I have been able to build my work without the fear of loosing track. Not everyone are granted such a great privilege. Please accept these humble words to express my gratitude to you.

Prof. Karl-Friedrich Klein, without your contributions and expertise I would not have been able to produce the great results in this study. I appreciate every minute that you spent helping me. Thank you.

Antti Heikkila, Markus Nordberg and Pekka Suominen, thank you for friendship, encouragements and all your help before and during the work at CERN.

Dr. Frederic Trillaud, thank you for the fruitful discussions that guided me in the beginning of designing my experiments.

The section leader Dr. Johan Bremer and the technicians at *cryogenics laboratory and instrumentation* at CERN, thank you for your expertise and patience with the most laborious project during my PhD.

Les techniciens Pierre-François Jacquot, Françis Beauvais et Sébastien Laurent, mes amis qui etaient aussi mes professeurs de Francais. Merci beaucoup! Merci pour tout les discussions inoubliables et vôtre aide sur mes expériences.

My friends Michiel de Rapper, Simone de Rapper, Aziz Zaghloul and Daniel Cookman's whole family, I miss you and the time that we spent together.

Tapani Rantanen ja Helmi Rantanen, *Mamma* ja *Pappa*, kiitos antamastanne tuesta ja uskosta tekemiseeni.

My parents Mikko Takala and Outi Takala, thank you for all your support, your care and all the important discussions that made me try my best.

My wife Silja Takala, you helped me with the proof reading of several publications and thesis. Especially I thank you for all the sacrifices that you have done for me.

This thesis is dedicated to my lovely wive. She has always been there for me. She left Finland with me to make me happy when I was obsessed to go to CERN. She made sacrifices in her life to make mine better. She woke up and poured me water in the middle of the night when I had an obsessive need to calculate or I had an idea. She brought me a snack at 2 am when I was obsessed to finish my measurements. No one has done more work for this book than you, not even me, I love you so much! It has been said that "I am not lucky, I am blessed", it is truly so, luck can not reach to this! I thank you Jesus, my God, for letting all this happen.

My beautiful son was born in September 2011 while I was still at CERN. You make my every day a happy day with your smile, I love you.

Contents

1 Introduction

The *Large Hadron Collider* (LHC), built and operated by CERN, the European Organization for Nuclear Research (Organisation européenne pour la recherche nucléaire), is the world's largest particle accelerator situated in France and Switzerland (for similar projects see table 1). It consist of 27 km long superconducting synchrotron and collider with four collision points and particle detectors. By colliding particles in the collision points with higher energy and luminosity than ever before, the LHC tries to answer questions in four categories: The origin of mass, matter-antimatter asymmetry, dark matter and dark energy, and the quark-gluon plasma [1, ch. 1].

The particles are accelerated to velocities close to the speed of light. The purpose of the superconducting magnets is to provide sufficiently high magnetic field over the beam pipes for guiding the charged, moving particles. The LHC consists of 1232 superconducting 14.3 m long twin dipole magnets, which can provide 8.3 T maximum field to keep 7 TeV particles in circular trajectory [1, ch. 4.1]. Figure 1 shows an artistic view of the twin dipole design inside the HeII cryostat, which is currently used in the LHC. The magnets are wound with NbTi Rutherford cables and cooled down to 1.9 K to reach the best performance of the superconductor. Figure 2 shows the cross-section and the transversal view of the Rutherford cable; and the single strand used in the cable. In addition to the cryodipoles, there are also quadrupoles to focus the beam and higher order harmonic magnets to correct the beam stability, yielding the total number of superconducting magnets of 1700 [4].

The two important features of the LHC are high luminosity and high beam energy. The more important feature is the beam energy since it defines which reactions are possible in the collision points. The luminosity, *i. e.* the parameter which defines the number of collisions in given time is given as follows

$$N_{\text{event}} = L\sigma_{\text{event}}, \tag{1}$$

where σ_{event} event is the cross section for the event under study and L is the machine luminosity. The luminosity depends only on the beam parameters and can be written for a Gaussian beam distribution as [6]

$$L = \frac{N_{\text{b}}^2 b_{\text{b}} f_{\text{rev}} \gamma_r}{4\pi\varepsilon_n \beta^*} F, \tag{2}$$

where N_{b} is the number of particles per bunch, b_{b} the number of bunches per beam, f_{rev} the revolution frequency, γ_r the relativistic gamma factor, ε_n the normalized transverse beam emittance, β^* the beta function at the collision point and F the geometric

a)

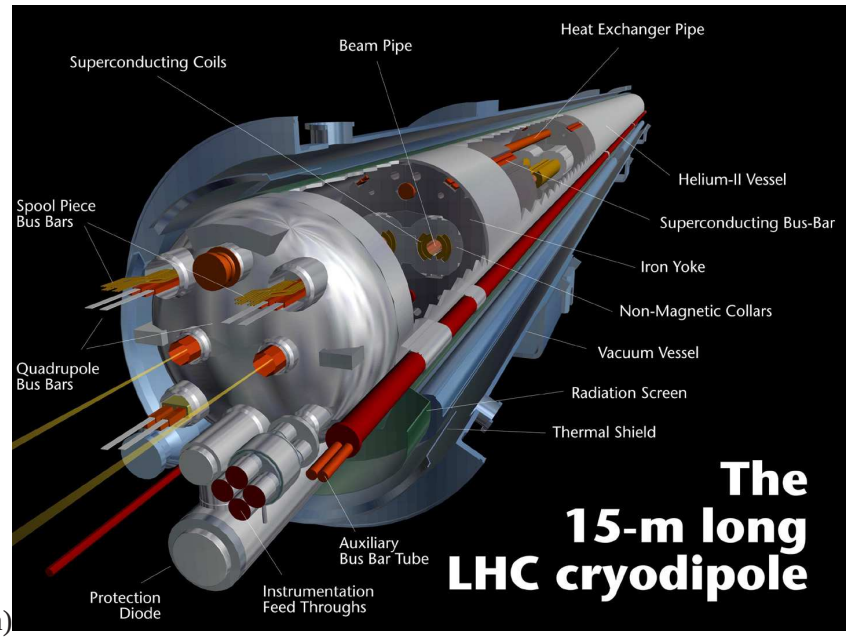

b)

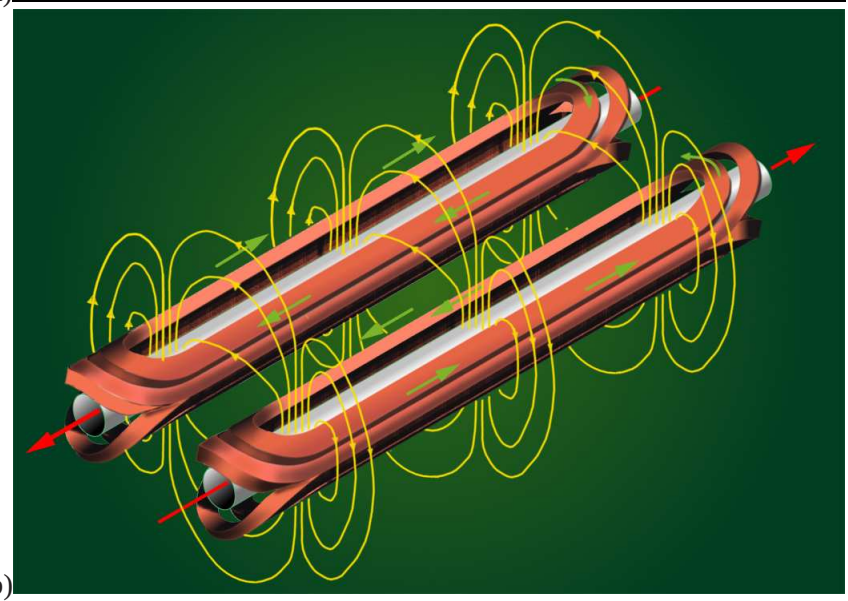

Figure 1. Artistic view of a) complete LHC twin dipole inside the HEII cryostat, with all its main components (courtesy of V. Frigo, CERN) [2]. The point of interest of this work lies in the superconducting coils. b) The magnetic field created by the superconducting dipole coil [3]. The red lines represent the beam direction, the green lines represent the direction of the current in the superconducting coils and the yellow lines represent the magnetic field generated by the supercurrent.

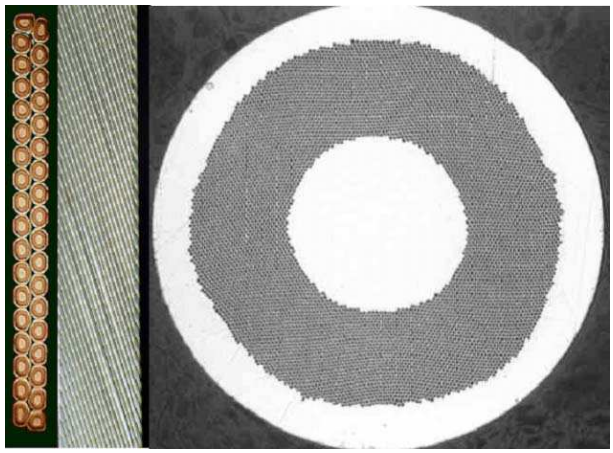

Figure 2. The Rutherford type of NbTi superconducting cable [4]. On the left hand side of the picture, there is the cross section of the cable, in the middle is the transversal view and on the right hand side there is a single NbTi strand which is used in dipole and quadrupole magnets. The gray area in the strand is the superconductor. Actually, it consist of several filaments which are from 6 μm to 7 μm of diameter, which is approximately ten times smaller than the diameter of a human hair.

Table 1. Main projects of hadron colliders [2].

Project (Lab)	Beam Energy (TeV)	B_{dipole}(T)	Tunnel (km)	Status
CBA[a] (BNL)	0.4	5	3.8	Shut down in 1983
Tevatron[b] (FNAL)	0.9	4	6.3	Operated since 1987
HERA (DESY)[c]	0.92	5.3	6.3	Operated since 1989
SSC (Dallas)	20	6.8	87	Cancelled in 1993
RHIC (BNL)	0.1/nucleon[d]	3.4	3.8	Operated since 1999
LHC (CERN)	7	8.3	27	Operated since 2008[e]

[a]Last name of the early "Isabelle".

[b]Operation of superconducting magnets began in 1983 at lower field.

[c]After upgrading in 1998 from 0.82 TeV, 4.7 T.

[d]Heavy ion accelerator.

[e]Not fully operational due to unstable interconnections between the magnets. Operated from 2010 with half of the designed beam energy, 3.5 TeV/beam [5].

luminosity reduction factor due to the crossing angle at the interaction point. The beam energy in synchrotron is given for relativistic particles roughly as follows [2]

$$E_{\mathrm{beam}} \approx 0.3 B_{\mathrm{dipole}} R, \tag{3}$$

where B_{dipole} is the magnetic field (in T) of the dipoles over the beam pipe and R (in km) is the effective radius of the synchrotron. Therefore, increasing the dipole field is as advantageous as increasing the radius in seeking for higher energies, and of course it is more practical. There are two projects for upgrading the luminosity and energy of the current LHC: 1. The *High Luminosity LHC* (HL-LHC) and 2. *the High Energy LHC* (HE-LHC) [7]. The first one is intended for increasing the luminosity of the LHC from $10^{34}\ \mathrm{cm}^{-2}\mathrm{s}^{-1}$ to $5 \cdot 10^{34}\ \mathrm{cm}^{-2}\mathrm{s}^{-1}$ [8, 9]. With magnet design one can affect the β^* function. From the equation (2) one can see that the value of the β^* function needs to be decreased in order to gain higher luminosity. The main idea of the project is to build quadrupole magnets with high aperture to get low β^* values. In the zero order the β^* is inversely proportional to the square of the aperture [7]. The magnets are relying on the Nb_3Sn superconductor technology. The target current is 1500 $\mathrm{A/mm}^2$ at 15 T for which the two candidate technologies, RRP (Restack Rod Process) from OST and PIT (Powder In Tube) from Bruker-EAS, are both considered. The cross-section of an RRP strand is shown in figure 3. The filament size, given by size of each of the 108 "islands" shown in figure 3, is much greater (50 μm) than in the NbTi case (6 μm to 7 μm, figure 2). The filaments cannot be made as small as in the NbTi because of the inherent fractures in the fabrication process. It is possible to produce Nb_3Sn strands with smaller filaments (bronze method), however they suffer from low critical current density. The HE-LHC project aims at higher beam energies. The equation (3) shows that the only practical solution is to increase the magnetic fields. The plan is to build a 20 T twin dipole with 40 mm bore. The design is ambitious, consisting of 11 different sections of superconductor wound with NbTi, 2 different type of Nb_3Sn and HTS wires [7]. One of the concerns in the new generation magnets is the stability of the high critical current Nb_3Sn superconducting strands [7]. The scope of this thesis is to contribute to the stability of these strands by expanding the scientific methods for characterizing the dominant effects and providing more information for the magnet technology in order to avoid the restricting effects since the stability of the strand is closely related to stability of the superconducting magnets [**P6**].

The importance of stability became evident in the famous incident of sector 3-4 on 19. September 2008 [10, 11, 12]. In the main dipole circuit of the LHC, the current was being ramped up to 9.3 kA during the commissioning of the magnets. At 8.7 kA an

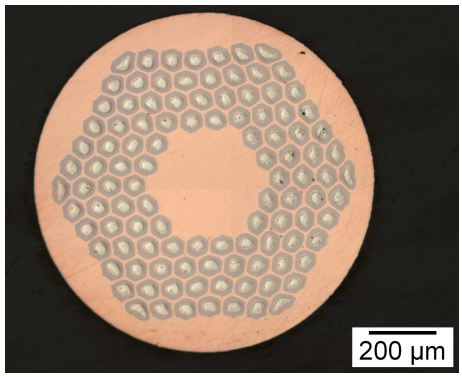

Figure 3. The crossection of a 0.7 mm RRP 108/127 from OST.

undetected resistive zone suddenly developed in one of the interconnects between two magnets [11]. The resistive zone resulted in an electric arc, dissipating 500 kW in the first tenth of second, and more than 4 MW after one second, causing mechanical damage in the magnets. It was concluded that the interconnection was faulty, too resistive, causing the thermal runaway. Approximately 2 tons of helium was rapidly discharged and eventually released to the tunnel in the first two minutes. The consequences of the incident were not only expensive but time consuming, delaying the LHC physics experiments. The damaged zone was over 755 meters long and encompassed 53 cryomagnets, where 30 of them had to be replaced by spares. One can imagine that repairing/replacing and reinstalling 15 meter long complex superconducting magnet systems 100 meters below the ground is not trivial. The stability is extremely diverse issue, and the incident explained above is initiated by so called thermal instability which is somewhat different to what is studied in this thesis. However, it is concrete example of the possible severe consequences of the superconductor instability accompanied with lack of magnet protection [13]. One should note, that it is possible to design a usable magnet also with a conductor that suffers from instabilities. In that case it is required that the magnet is not driven to the unstable regions and it should be well protected against quenching. The disaster could have been avoided by paying more attention for protecting the interconnects. Otherwise, there are numerous examples of less significant events in the history, where the stability of the superconductor is shown to restrict magnets from working in their nominal operating currents. In fact this issue has been following the magnet technology from the very first magnets and it will always be one of the important aspects to look at when new performance boundaries are pursued.

Although the Nb_3Sn RRP superconducting strand is foreseen to be used in the next

generation magnets, there are still stability issues in them. The strand has been studied as a single strand [14, 15, 16, 17], in cables [18][**P7**] and in magnets [**P6**]. It has been shown that the so called Magneto-Thermal Instability (MTI) can cause premature quenches in strands that have high critical current density (J_c). There have been several studies of the stability in this category [19, 20, 21, 22], [13, ch. 7]. However, there haven't been any experimental studies to characterize the perturbation sensitivity of the MTI, since it requires a novel technique which has not existed before. The main experimental focus of this thesis is to further develop a recently introduced principle of a novel technique so that it is optimized for studying the perturbation sensitivity of the MTI in high J_c Nb_3Sn superconducting strands and to use it to characterize a 0.7 mm RRP 108/127 strand which is one of the essential strand types for the next generation accelerator magnets. Before entering more into the details of the Magneto-Thermal Instability, the relevant fundamentals of the superconductivity are introduced to the reader.

2 Superconductors

Superconductivity was discovered in 1911 by Karmelingh Onnes while he was studying the resistivity of mercury at cryogenic temperatures [23, ch. 18]. Superconductivity is an electro-magnetic property which emerges in certain conductors under suitable conditions. To reach the superconducting state in superconducting material the temperature, magnetic field and current density need to be lower than the critical values: *critical temperature* T_c, *critical magnetic flux density* B_c and *critical current density* J_c. Otherwise the material is in the *normal state*. In the superconducting state the DC electric resistivity is zero and the magnetic susceptibility is -1 [24, ch. 10.1]. Superconductor is an ideal conductor and diamagnet: electric current never decays in a superconductor and magnetic fields are repelled from it (*Meissner-Ochsenfeld effect*). The critical field can be expressed in terms of Gibbs free energy between normal G_n and superconducting G_s states [25, p. 342]

$$G_\mathrm{n} - G_\mathrm{s} = \frac{B_\mathrm{c}^2}{2\mu_0}. \tag{4}$$

The BCS-theory The superconducting state is explained by the BCS-theory [26]: The interaction between two electrons via lattice vibration is attractive for two electrons with opposite momenta, whose energies lie within $\hbar\omega_\mathrm{D}$ (ω_D is the Debye's frequency) from the fermi energy. The two electrons with opposite spin and momentum form a bound boson type quasi-particle called a *pairon* (also *cooper pair*) which is free to move in the lattice [27, ch. 3]. If too high fields (T,B or J) are present the pairons are broken and superconducting state is lost. One of the great success of BCS theory was the evaluation of the T_c in terms of the energy gap and basic parameters, and the prediction of the isotopic effect (which confirms the critical role of the lattice) [25, p. 342]

$$T_\mathrm{c} = \frac{\Delta_0 e^\gamma}{\pi k_\mathrm{B}}, \tag{5}$$

where Δ_0 is the zero temperature band gap, γ is the Euler-Mascheroni constant, and k_B is the Boltzmann constant.

The Ginzburg-Landau equations There are two types of superconductors, called type I and type II, which can be explained by the phenomenological Ginzburg-Landau (GL) theory [27, ch. 10]. The GL-theory, worked out well before the microscopic BCS theory (GL 1950, BCS 1957). It can be derived from the BCS-theory [28] and provides a good description for the properties of the two types: The Gibbs free energy of the

superconducting state was written as a function of a complex *order parameter* Ψ' and magnetic vector potential A (with quantum replacement). The order parameter represents the pairon wave function. The free energy was minimized with respect to Ψ' and A, which leads to *Ginzburg-Landau equations*.

Two important coefficients can be derived from the theory: the *coherence length*

$$\xi^2 = \frac{\hbar^2}{2m^* |a|} \tag{6}$$

and the *London penetration depth*

$$\lambda_{\mathrm{L}}^2 = \frac{m^*}{\mu_0 e^{*2} |\Psi'|^2}, \tag{7}$$

where m^* is the effective mass of the pairon, $e^* = 2e$ is the charge of the pairon; λ_{L} is a temperature dependent parameter. Before Ginzburg-Landau equations, the London penetration depth was already derived from London equations [29].

Superconductor type II for high fields The ratio of the two coefficients

$$\kappa = \frac{\lambda_{\mathrm{L}}}{\xi} \tag{8}$$

divides the superconductors in the two categories [30, ch. 4]: type I when $\kappa \leq 1/\sqrt{2}$ and type II when $\kappa \geq 1/\sqrt{2}$. Instead of one critical magnetic field density, the type II superconductor has two critical fields

$$B_{\mathrm{c}_1} = \frac{\Phi_0 \ln \kappa}{4\pi\lambda_{\mathrm{L}}^2} \tag{9}$$

and

$$B_{\mathrm{c}_2} = \frac{\Phi_0}{2\pi\xi^2}, \tag{10}$$

where $\Phi_0 = h/e^*$ is the quantum of flux (also fluxon). The magnetic properties of the type II superconductors can be explained via the GL theory [31]. Below the first critical field, Meissner-Ochsenfeld effect dominates and the conductor is in the Meissner phase. Surface energy of the type II superconductor is negative and in between the two critical fields the so called Abrikosov's flux line lattice penetrates the superconductor without vanishing completely the superconducting state. The flux lattice consist of *vortices*, small volumes in the superconductor in where a fluxon is able to penetrate through the material. The vortex consists of a normal core (of radius ξ) and an outer

part (of radius λ_{L}) where screening currents circulate around the core. A superconductor with Abrikosov's flux line lattice is said to be in the *Shubnikov phase* or the *mixed state*. The magnetic flux enclosed in the vortices is quantized. The B_{c} is also referred as the *thermodynamic critical field* and can be expressed as [25, p. 342]

$$B_{\mathrm{c}} = \frac{\Phi_0}{2\sqrt{2}\pi\lambda\xi}, \tag{11}$$

and thus the upper and lower critical fields may be expressed as

$$B_{\mathrm{c}_1} = \frac{B_{\mathrm{c}} \ln \kappa}{\sqrt{2}\kappa} \tag{12}$$

and

$$B_{\mathrm{c}_2} = \sqrt{2}\kappa B_{\mathrm{c}}. \tag{13}$$

Hard superconductors If a type II superconductor is in the mixed state and a current is applied, the electro-magnetic force

$$\vec{f}_{\mathrm{L}} = \vec{J} \times \vec{\Phi}_0, \tag{14}$$

where $\vec{\Phi}_0 = \Phi_0 \frac{\vec{B}}{B}$, acts on the Abrikosov's flux lattice [32, ch. 1.1]. Therefore, flux motion is induced in the material which dissipates energy and thus potential difference must be applied in order to maintain the current. If the superconductor has defects in its crystal structure, the vortices are *pinned* and the flux motion is eliminated. The pinning means that the vortices are locked in *pinning centers*, which are microscopic volumes of superconducting material where the κ is depressed or volumes of non-superconductive material. The pinning centers can be made also artificially for example by doping the material [33]. Type II superconductors can withstand remarkably high magnetic fields, *e. g.* B_{c_2} can be several hundred Teslas in high-temperature superconductors. The type II is divided in two subcategories depending on their pinning strength: *soft* and *hard superconductors*. The latter have much stronger pinning. For *extremely hard superconductors* $D_{\mathrm{t}}/D_{\mathrm{m}} \approx 0$ [34], where magnetic diffusion coefficient

$$D_{\mathrm{m}} = \frac{\rho_{\mathrm{n}}}{\mu_0} \tag{15}$$

and thermal diffusion coefficient

$$D_{\mathrm{t}} = \frac{k}{\gamma C}, \tag{16}$$

where ρ_{n} is the normal state resistivity, k is the heat conductivity, C is the mass heat capacity of the material and γ is the density. Usually high ρ_{n} is a prerequisite for hard superconductivity: indeed high normal state resistance means strong interaction between

electron and lattice which can lead to strong coupling between electron, mediate by electron-phonon interaction. The hard, type II superconductors are used in superconducting magnets for their auspicious properties, *e. g.* one of the oldest and most interesting superconductor Nb_3Sn which is the conductor of interest in this thesis.

Critical-state model Bean's model [35, 36], later generalized by Kim et al [37], describes the *critical-state model* of hard super conductors: the density of supercurrent in superconducting material is always zero or the critical current density $J_{\mathrm{c}}\left(B,T\right)$ which is dependent on magnetic field density and temperature; and independent of the macroscopic electric field. The critical state model is well verified in all practical superconductors and it is the base for all phenomenological theory describing the behavior of high current density superconductor, including the more recent superconductors, like the ceramic copper oxides (1986) and the magnesium diboride (2001) superconductors.

3 Magneto-thermal instability

The critical state can be problematic in hard superconductors when the critical current is high. An irreversible sudden transition from superconducting to normal state may arise due to a local perturbation in magnetic or thermal state of the superconductor. After the transition, the normal zone generates more heat since the current flows through it. Thus, if there is enough magnetic energy, the normal zone may propagate until the superconductor is completely normal. This phenomenon is called the *quench*. For example, during a quench in a superconducting magnet the normal state diffuses all around the superconducting matter and all the magnetic energy of the magnet is dissipated as heat. The quench can happen at current well below the values expected form the critical surface of the conductor. In magnets the quench currents may be improved by *training*, which encompasses several consecutive quenches and thermo cycles. The maximum current can usually be improved drastically from the first quench, depending on the mechanical quality of the magnet. For example superconducting quadrupoles were tested with filled and unfilled epoxy resin impregnation [38]. The used strand was confirmed with 100% of the nominal critical current in short sample tests. The training of the test magnets yielded improvements from 63% to 98% and from 39% to 90% of the nominal critical current for silica-filled and unfilled epoxies, respectively.

In the old days quenches were not expected and one explanation proposed for the degraded currents was a weak spot in the conductor, nevertheless it could not explain the training effect [13, ch. 5]. *Perturbation spectrum* (also disturbance spectrum) is used to encompass all the perturbations as a magnet is energized. The most important part of the spectrum, the perturbations which are local and transient, arises from the frictions and mechanical stress due to the electro-magnetic forces. Usually magnets are not mechanically fine tuned to support the ensemble due to some weak areas which give in when the stress is applied for the first times. Every time the magnet is energized, the weak areas settle down as they give in, *i. e.* the mechanical fine tuning is done by the training the magnet. Thus, the change in the perturbation spectrum can explain the training effect in case of transient localized perturbations. There are several possible perturbations: continuous (bad joint), distributed (variable field losses, heat leak, mechanical hysteresis) and transient perturbation (e.m. forces and frictions and/or flux jumping) [13, ch. 5]. Usually the mechanical perturbations are the most serious problem, however when the J_c is high, *flux jumping* may become a limiting factor. It is a vicious circle, which may be initiated by adding heat to the system in a short period of time (perturbation). The heat release increases the temperature which in turn reduces the critical current density.

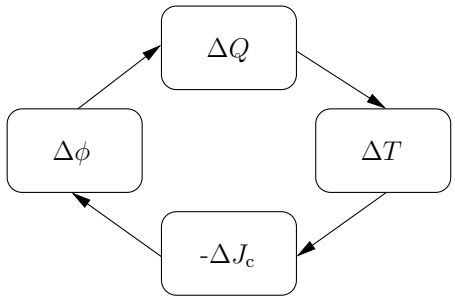

Figure 4. The vicious circle of flux jumping [13, ch. 7].

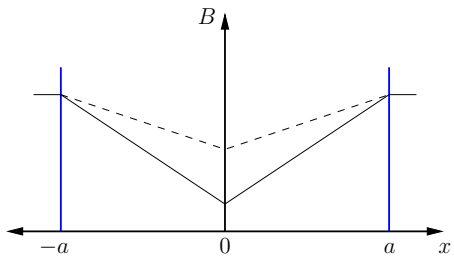

Figure 5. The magnetic field distribution before and after the heat input, changing the J_c value due to temperature increase, in a fully penetrated superconducting slab according to the adiabatic theory of flux jumping [13, ch. 7].

Thus, the magnetic flux is obliged to change profile as stated by the Ampère law and the Bean Model. The change in magnetic flux generates more heat, and the circle is closed with a positive feed back (figure 4). The process can continue until the magnetic energy is dissipated. Mathematical analysis of flux jumping requires investigating the stability of the electromagnetic (Maxwell) and heat diffusion equations.

3.1 Adiabatic theory of flux jumping

In [13, ch. 7] the stability of a superconducting slab is analyzed quantitatively. The slab is fully penetrated by applied magnetic field and thus screening currents are induced. A small quantity of heat is added to the system which is assumed to be adiabatic. The Bean model is assumed, therefore when the temperature rise is observed the screening currents will enter to the flux flow regime and start to decay, generating more heat and leaving a new field pattern (see figure 5)

$$\Delta q\left(x\right)=\int I\left(x\right)E\left(x\right)\mathrm{d}t=J_{\mathrm{c}}\Delta x\Delta\phi\left(x\right), \tag{17}$$

where x is the coordinate of the slab in the direction of the width, $\Delta q\,(x)$ is the change in heat energy density, $I\,(x)$ is the current in a slice Δx, $E\,(x)$ is the electric field and $\Delta\phi\,(x)$ is the change in magnetic flux. The heat energy per unit volume of the slab is then

$$\Delta Q = \mu_0 J_\mathrm{c} \Delta J_\mathrm{c} \frac{a^2}{3}, \tag{18}$$

where ΔJ_c is the change in critical current density due to the increase in temperature and a is the slab half-width. The Bean model

$$\frac{\partial J_\mathrm{c}}{\partial T} = -\frac{J_\mathrm{c}}{T_\mathrm{c} - T}, \tag{19}$$

and simple heat balance equation yields a stability parameter

$$\beta = \frac{\mu_0 J_\mathrm{c}^2 a^2}{\gamma C\,(T_\mathrm{c} - T_0)} < 3, \tag{20}$$

where T_0 is the initial temperature of the slab. This stability condition will make sure that the slab is stable against flux jumping according to the adiabatic theory of flux jumping. If the eqn. (19) is not used but the B dependency of the current density is still neglected, the criterion is the same as was obtained earlier in [39, ch. 4.7.3.2]

$$\frac{J_\mathrm{c}^2 a^2}{4} < \frac{3}{\mu_0} \gamma C \left(\frac{-J_\mathrm{c}}{\frac{\partial J_\mathrm{c}}{\partial T}} \right). \tag{21}$$

The important implication of this theory comes from the strong influence of superconductor width on the stability parameter. It is recommended to use fine degree of subdivision of superconducting matter in strands as presented in figure 3, which is especially important when the J_c is high. Moreover, it is advantageous to increase the heat capacity of the conductor. However heat capacity depends basically on the operating temperature, which for high J_c superconductors is only 4.2 K or, even worst, 1.9 K. Use of *High Temperature Superconductors* (HTS) may be advantageous also at 4.2 K because of flat temperature/field dependency of current density. The summary of the relevant strand attributes and their effect on stability is presented in table 2.

3.2 Magnetization instability

The adiabatic theory of flux jumping presented above describes well the fundamental idea of instability of a magnetized superconducting filament. This type of an instability is called the *magnetization instability* (also *magnetic instability*) and it is considered the first kind of *Magneto-Thermal Instability* (MTI). The basic equations (20) and (21) of

Table 2. Relevant strand attributes and their effect on stability according to the adiabatic theory of flux jumping.

Attribute	Effect on stability
Width	$\propto 1/a^2$
Critical current density	$\propto 1/J_{\mathrm{c}}^2$
Heat capacity	$\propto C$

the adiabatic theory are criteria for stability in strict sense and do not always describe the magnetization instability in the wide sense. The strict criteria guarantees absolute stability for the superconductor, *i. e.* flux jumping is not allowed to happen at all. However, the most important criterion is the quench criterion (wide sense) which allows flux jumping if it doesn't result in a quench. Therefore, the strict sense of the criterion is not convenient in some cases [40] when the actual consequences of the stability is of interest.

3.2.1 The wide criterion for magnetization instability

A stability criterion in the wide sense for the magnetization instability in hard superconducting strands is presented in [20]. The critical state model is assumed and the effect of self-field on the critical current density is neglected. More restrictive assumption is made on the magnetic diffusivity which is assumed larger than the thermal diffusivity, however for hard superconductors this is not an issue. The round filaments are approximated with squares of the same area and the heat generation is assumed to increase the internal energy of the filaments without changing the volume or pressure. By following similar analysis to [39, ch. 4.7.3.2], the change in heat energy in adiabatic system due to flux movement is [20]

$$\Delta Q = \frac{1}{2a}\Big|_{-a}^{a} E_z^* H_y - \Delta \overline{W}_{\mathrm{m}}, \tag{22}$$

where E_z^* is the time integral of the electric field along the superconductor from the initial to final state, H_y is the applied magnetic field and $\overline{W}_{\mathrm{m}}$ is the average energy stored in the magnetic field inside the filament. The essential idea of the model is the *enthalpy stabilization criterion* [41] in small scale (strand vs. magnet). The strand is considered unstable if the magnetic energy dissipation is enough to increase the temperature of the

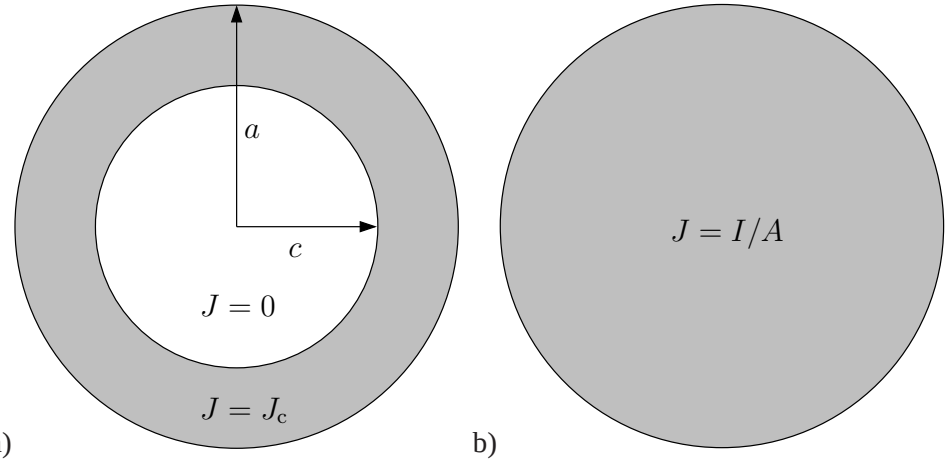

Figure 6. The current distribution in a round superconducting strand. a) Before flux jump and b) final distribution.

superconductor over the T_{c}. Thus the enthalpy stabilization criterion is

$$\Delta Q < \Delta U(B, T_0, \Delta T_{\mathrm{e}}), \tag{23}$$

where ΔT_{e} is the temperature rise from the initial temperature T_0 to T_{c}. The change in internal energy of the strand is defined as

$$\Delta U(B, T_0, \Delta T) = \int_{T_0}^{T_0+\Delta T} C_{\mathrm{p}}\,(B, T)\,\mathrm{d}T, \tag{24}$$

where C_{p} is the average heat capacity for copper stabilizer/superconductor mixture and ΔT is the temperature rise. Thus, a strand can be stable against magnetization instability even though it doesn't fulfill the adiabatic flux jumping criteria. It means that in enthalpy stabilized superconducting strands *partial flux jumps* may be observed. A partial flux jump is an initiated flux jump which doesn't result in a quench.

3.3 Self-field instability

In [13, ch. 7] the adiabatic theory of flux jumping is applied to a multi filamentary strand. It is assumed that initially, the current flows in the outermost filaments of the strand, see figure 6 a. The thickness of the current layer is defined by the ratio of the current carrying capacity, *i. e.* I_{c}, and the transport current. The energy per unit volume is

$$\Delta Q = \mu_0 \lambda^2 J_{\mathrm{c}} \Delta J_{\mathrm{c}} a^2 \left(-\frac{1}{2}\ln\varepsilon - \frac{3}{8} + \frac{\varepsilon^2}{2} - \frac{\varepsilon^4}{8} \right), \tag{25}$$

where λ is the fill ratio of the superconductor and $\varepsilon = c(\lambda J_\mathrm{c}, a)/a$ is the relative thickness of the current layer. The stability parameter in strict sense is then

$$\beta_t = \frac{\mu_0 \lambda^2 J_\mathrm{c}^2 a^2}{\gamma C \left(T_\mathrm{c} - T_0\right)} < \left(-\frac{1}{2}\ln\varepsilon - \frac{3}{8} + \frac{\varepsilon^2}{2} - \frac{\varepsilon^4}{8}\right)^{-1}. \tag{26}$$

One should note that in this form it is not immediately clear what is the influence of J_c and a on the stability since the ε on the right hand side of the inequality is dependent on both of them. The self-field instability is considered the second kind of MTI.

3.3.1 The strict criterion for self-field instability

In addition to the adiabatic flux jumping theory there is another type of criterion in strict sense of the stability, the implications of the theory are similar with somewhat different equations. The theory considers the stability of a multi filamentary composite against a small perturbation. In [34] the analysis for calculating the stability criterion for a composite follows the formulation presented in [42], which is generalized for any $D_\mathrm{m}/D_\mathrm{t}$. For a small perturbation the heat equation may be linearized with respect to θ as

$$\gamma C \frac{\partial \theta}{\partial t} = k\nabla^2\theta + J_\mathrm{c} E \tag{27}$$

where θ is a small elevation in the superconductor temperature, $\theta \ll T_\mathrm{c} - T_\mathrm{i}$, T_i is the initial temperature after the perturbation, $J_\mathrm{c} = J_\mathrm{c}(T_\mathrm{i})$ and E is the electric field arising during the flux motion. The constitutive equation for electric field is written as follows

$$J = J_\mathrm{c}\left(T\right) + \frac{E}{\rho_\mathrm{n}}, \tag{28}$$

which is fair only if the current density is well above the critical value when most of the electric field is caused by the normal part of the conductor. To the first approximation with respect to θ the eqn. (28) is

$$J = J_\mathrm{c} + \frac{\partial J_\mathrm{c}}{\partial T}\theta + \frac{E}{\rho_\mathrm{n}}. \tag{29}$$

For electric field, the Maxwell-Faraday equation and the Ampère's circuital law yields

$$\nabla \times \nabla \times E = -\mu_0 \frac{\partial J}{\partial t}. \tag{30}$$

It is assumed that the Bean model is applicable, eqn. (19). The Bean-Livingstone's surface barrier [43] is assumed to be absent *i. e.* when the applied magnetic field is sufficiently high the flux is free to propagate through the surface. As an electro dynamical

boundary condition, the applied magnetic field is constant. The analysis for round superconducting strands starting from the equations above are done for isothermal cases with and without normal metal ($\rho_{\mathrm{n}} < 10^{-7}\Omega$m) coating [21]. The analysis yields

$$\frac{\mu_0 R^2 J_{\mathrm{c}}}{C_{\mathrm{V}}} \left| \frac{\partial J_{\mathrm{c}}}{\partial T} \right| < \gamma^2 (I) , \tag{31}$$

where R is the strand's radius and γ is the stability parameter. With help of eqn. (19) it is convenient to write

$$R_0 = \sqrt{\frac{C_{\mathrm{V}} (T_{\mathrm{c}} - T)}{\mu_0 J_{\mathrm{c}}^2}}, \tag{32}$$

since the eqn. (31) may be expressed as

$$\frac{R}{R_0} < \gamma (I) , \tag{33}$$

where the stability parameter $\gamma (I)$ is determined from the equation

$$N_1 (\gamma) J_0 (\rho) - N_0 (\rho\gamma) J_1 (\gamma) = 0 \tag{34}$$

for a strand without coating and

$$N_0 (\gamma) J_0 (\rho) - N_0 (\rho\gamma) J_0 (\gamma) = 0 \tag{35}$$

for a strand with coating, where J_0, J_1 and N_0, N_1 are Bessel functions of first and second kind. The stability in both cases are represented in figure 7. The equations and the figure show four important remarks: 1) the strand is more stable if it is coated with metal, 2) the stability is inversely proportional to the radius of the strand, 3) as well as to the critical current density and 4) proportional to the square root of heat capacity. The table 3 summarizes the discussed results. The effect on stability is a square root of the results presented in table 2 for the adiabatic theory of flux jumping. The coating with metal is practically always fulfilled: all strands have the external crust (outer 10 μm) only of stabilizing material without superconducting filaments.

3.3.2 The wide criterion for self-field instability

The adiabatic flux jumping theory is extended in [44, 45] to a quench criterion. The basic idea of the criterion is the same enthalpy stabilization principle as presented in section 3.2 for magnetization instability. In case of an initiated self-field instability, the

Table 3. Relevant strand attributes and their effect on self-field stability according to the strict criterion.

Attribute	Effect on stability
Normal metal coating	Increase
Radius	$\propto 1/R$
Critical current density	$\propto 1/J_{\mathrm{c}}$
Heat capacity	$\propto \sqrt{C_{\mathrm{V}}}$

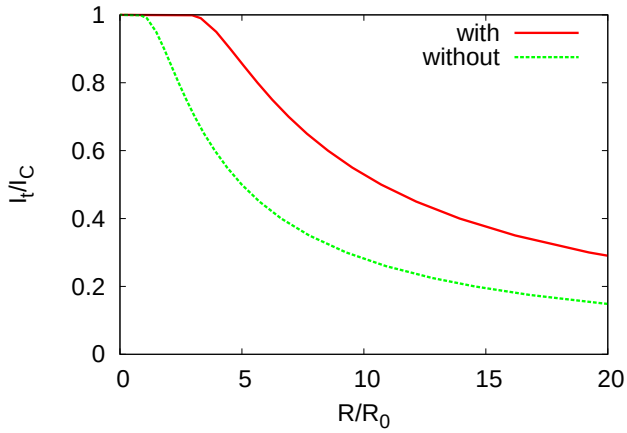

Figure 7. The stability of superconducting strand with isothermal boundary conditions. I_{c} is the critical current and I_{t} is the transport current.

current moves towards the innermost filaments. If the flux jumping continues to the final state, the current is uniform over the strand cross section, see figure 6 b. During the process energy dissipates as heat. The dissipated heat energy associated with the flux movement is called the self-field energy. The strand is considered unstable if the self-field energy is enough to increase the temperature of the superconductor over the T_{c}. The lowest current which fulfills the criterion, is called the *minimum quench current* with respect to the self-field instability. It should be noted that there is a mistake in the equation of the self-field energy in [44, 45]. It is given as follows

$$\Delta Q = -\mu_0 \lambda \frac{I^2}{\pi} \int_{\varepsilon_0}^{\varepsilon_{\mathrm{f}}} \left(-\frac{1}{2}\ln\varepsilon - \frac{3}{8} + \frac{\varepsilon^2}{2} - \frac{\varepsilon^4}{8} \right)^{-1} \mathrm{d}\varepsilon, \tag{36}$$

containing an extra λ, while it should be

$$\Delta Q = -\mu_0 \frac{I^2}{\pi} \int_{\varepsilon_0}^{\varepsilon_{\mathrm{f}}} \left(-\frac{1}{2}\ln\varepsilon - \frac{3}{8} + \frac{\varepsilon^2}{2} - \frac{\varepsilon^4}{8} \right)^{-1} \mathrm{d}\varepsilon. \tag{37}$$

The mistake doesn't change drastically the equation, since the λ is defined as the filling ratio in the filament region, where the copper content is small in the first place. However, the model now gives more accurate results [46]. One should note that the ε is dependent on the λ, and therefore it is a relevant parameter to the stability even according to the corrected equation.

The self-field instability arises from an uneven current distribution. As said, the current flows initially at the outermost filaments and then homogenizes over the strand cross section during the flux jump. However, it should be noted that in a more accurate review this criterion is simplifying the current distribution: current is carried by SC filaments only and not by the adjacent copper matrix. In reality the current is in the outermost filaments. When the instability is triggered the current redistributes from the filaments into the copper which also contributes to the self-field energy, otherwise the energy would be zero near the I_{c} which it is not (to be shown experimentally in section 9). Recently at CERN, a *Finite Element Method* (FEM) model was developed to theoretically study the self-field instability of the high J_{c} superconducting strands [22]. The uneven distribution between the filaments and the copper is taken into account in this FEM model.

3.4 The hypothesis and conventional measurements

In [45] the strict and the wide criteria are unified to one theory (review in [**P4**]) of the self-field instability in superconducting strands. The theory states that there are two

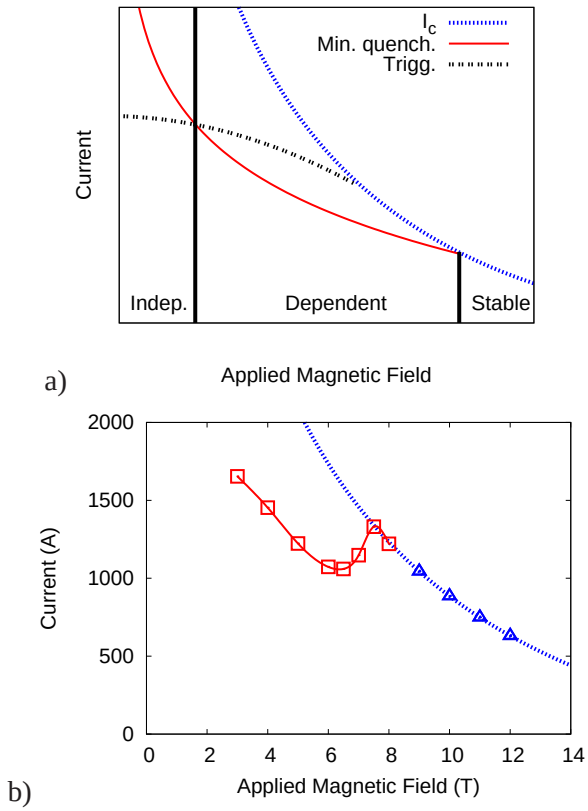

Figure 8. a) A sketch of the triggerable current and minimum quench current curves; perturbation independent, dependent and stable regions. b) Example of the minimum quench current line and conventional measurements. (▵) represent the critical current measurements, (····) is the critical surface, (▫) represent the quench current by natural perturbation in V-I measurements [**P4**].

current levels, which are defined by the strict and the wide criteria: 1. the *triggerable current* and 2. the minimum quench current, see figure 8 a. If the current is higher than the triggerable current, the self-field instability may be triggered by a small perturbation. However, only if the current is higher than the minimum quench current the instability may result in a quench. The FEM model mentioned above [22], was used to show that the triggerable current is actually a function of the perturbation energy. The higher the magnetic field, the larger needs to be the perturbation energy. Therefore, three different regions are defined: 1. the *perturbation independent*, 2. the *perturbation dependent* and 3. the *stable region* (with respect to the MTI), see figure 8 a. The boundary point between the perturbation independent and dependent regions shall be called

as the *perturbation region boundary* (PRB). The triggerable current depend on perturbation energy, so the "Trigg." curve of figure 8 may move up or down (the shape might change as well) according to the natural perturbation which is acting on the wire. The PRB therefore can move right or left. However the boundary between the perturbation dependent and the stable regions does not depend on the perturbation spectrum, it is a characteristics of the wire. In the perturbation independent region the triggerable current is lower than the minimum quench current and thus the strand quenches immediately if the current exceeds the minimum quench current. In the perturbation dependent region the triggerable current is higher than the minimum quench current and depend on the trigger energy. Thus when the self-field instability is triggered, it results in a quench. In the stable region the self-field energy is not high enough to quench the strand. However, one should note that even in the stable region the thermal instabilities, the ones where the external perturbation energy and the ohmic heating from the stabilizer are the only source of heat, might exist and might drive the magnet into quench.

It should be noted that the definitions of the perturbation dependent and independent regions described above are not unique with respect to the perturbation energy since they depend on the intersection of the triggerable current and the minimum quench current curve. In [**P4**] the *practical trigger limit* E_ε was defined to distinguish the relevant and insubstantial perturbation energies. Only the energies $> E_\varepsilon$ are considered relevant. Now, the perturbation dependent and independent regions are unique with respect to the perturbation energy. It is convenient to set the E_ε to the level of the natural perturbation of the system, which arises mainly from the electro-magnetic forces as the strand is energized. Thus, the E_ε can vary among the different measurements.

The *critical current* (I_c) and *stability current measurements* are the conventional way [14, 15, 16, 17][**P8**] of characterizing superconducting strands. The critical current measurement is done at constant magnetic field and temperature by ramping up the current until the critical current of the strand is reached. Normally, by means of these measurements the critical surface of the material is determined. However in the very high J_c wires, usually at field sufficiently lower than the critical field the sample quenches often prematurely well below the expected critical value: such a value is considered as *quench current* and not as part of the critical surface. The stability measurements are done exactly in this region, where the critical current is not reached due to premature quenching. In V-I stability measurement the magnetic field is kept constant while the current is ramped up until the strand quenches whereas in V-H stability measurement the magnetic field is ramped up and the current kept constant. The strand is quenched

several times in order to get the lowest possible value since there is some variation between the measurements due to spread of the natural perturbation spectrum. The V-I is mainly for studying the self-field instability and the V-H for the magnetization instability. Prior to every measurement, the sample should be *magnetically cleaned, i. e.* quenched to remove the magnetic flux [45].

Figure 8 b shows an example of the conventional characterization of a 0.7 mm RRP 108/127 strand at 1.9 K. The measurement is conducted from 12 T to 0 T. The critical current is reached actually from 12 T to 8 T: below this range the highest current values no longer follow the critical surface which obeys a certain scaling law typical to the material and the production process. Premature quenching is observed below 8 T. The quench current is close to the critical surface between 8 T and 7.5 T. At fields from 7.5 T and 6 T the quench current decreases rapidly and then it increases monotonically when the field is further decreased below 6 T. According to the theory, quenching is triggered by the natural perturbation of the system. At fields higher than 6 T, the quench current is above the minimum quench current curve. Thus the PRB defined by the practical trigger limit is at 6 T. In the perturbation dependent region the natural perturbation is not strong enough to trigger the self-field instability at fields higher than 8 T. However, according to the theory [22] it should be possible to trigger a quench driven by the self-field instability mechanism even at higher fields than 8 T if the trigger energy is stronger than the E_{ε}. There are two examples which are supporting the hypothesis:

1. In [**P6**] a similar sample (with 54/61 sub-elements) was measured at 1.9 K. The sample mounting was such that the natural perturbation was too high for reaching the critical current at any field up to 12 T. After the measurement, the sample was glued to its sample holder in a way that the heat transfer with the helium bath was retained. Now, supposedly the level of the perturbation was lower due to the reduced micro movement and the sample was measured again with a remarkable effect. The critical current was reached at 11 T and 12 T; the PRB was at 7 T. 2. In [**P3**] a 0.8 mm RRP 54/61 was measured at 4.3 K. The sample was stable at fields 10 T-12 T and the PRB was at 3 T. The sample was remeasured with another type of sample holder and the critical current was not reached at all; the PRB was moved to 8 T. Supposedly, in both of these examples the level of natural perturbation was different between the two measurements which leads to different quench behavior. These measurements provide strong support for the theory. However, without being able to control the level of perturbation in the strand, it is difficult to put the theory into a rigorous test. Therefore it is necessary to build an apparatus for delivering a controlled energy deposition in the strand.

Thermal stability is closely related to the MTI and it is actually the final mechanism that takes control after the MTI has played its part as a quench initiation mechanism. First in the next two subsections the definitions are cleared out. After them the seek for the suitable energy deposition delivery system is presented.

3.5 Thermal stability

In a superconducting strand a normal zone may be induced by locally heating the strand to a sufficiently high temperature. The normal zone generates heat as the current flows through it. Thus the zone may propagate if it is not cooled down more efficiently than the heat is generated. The *Minimum Propagating Zone* (MPZ) is the length of a normal zone, that will grow without bounds, *i. e.* result in a quench. In adiabatic assumption, where cooling of the strand by the surroundings is not taken into account, the minimum propagating zone may be calculated for superconducting strands as follows [13, ch. 5]

$$l_{\mathrm{MPZ}} = \sqrt{\frac{2k\left(\theta_{\mathrm{c}} - \theta_0\right)}{J_{\mathrm{m}}^2 \rho_{\mathrm{m}}}}, \tag{38}$$

where J_{m} is the current density in the copper stabilizer and ρ_{m} is the resistivity of it. The *Minimum Quench Energy* (MQE) is the lowest limit for the energy which is needed to initiate an MPZ. In conventional MQE measurements the heater is considered to be the only contribution for creating the MPZ

$$\mathrm{MQE} = \pi r^2 l_{\mathrm{MPZ}} \int_{T_0}^{T_{\mathrm{c}}} C_{\mathrm{V}}(T)\mathrm{d}T. \tag{39}$$

This is called the thermal stability [13, ch. 5]. If the cooling is taken into account, a cooling term may be added to the eqn. (38) [47]. In magnets the MPZ can be extremely complex compared to the single strands. As presented in [48] one needs to take into account four different thermal phenomena: 1. The longitudinal propagation, as in strands; 2. transverse diffusion within the conductor; 3. diffusion through the insulating medium between conductors and 4. diffusion in the layer insulation.

3.6 Stability type criterion

In the adiabatic assumption, the heat energy that will cause an MPZ in superconducting strand is a sum of the two terms

$$\mathrm{MQE} = \Delta Q_{\mathrm{h}} + \Delta Q_{\mathrm{MTI}}, \tag{40}$$

where ΔQ_{h} is the trigger energy of an external source, for example a quench heater and ΔQ_{MTI} is the energy due to the MTI, *i. e.* the magnetization or self-field energy. Thermal stability and magneto-thermal stability can be distinguished by the following criteria: let us define

$$\alpha_{\mathrm{MTI}} = \frac{\Delta Q_{\mathrm{MTI}}}{\mathrm{MQE}}, \tag{41}$$

now the instability is purely thermal when $\alpha_{\mathrm{MTI}} \to 0$ and purely magneto-thermal when $\alpha_{\mathrm{MTI}} \to 1$. For finding the stability type, the eqns. (40) and (41) yield

$$\alpha_{\mathrm{MTI}} = 1 - \frac{\Delta Q_{\mathrm{h}}}{\mathrm{MQE}}, \tag{42}$$

where the MQE can be calculated from the eqns. (38), (39) and the ΔQ_{h} can be measured with *Minimum Trigger Energy* (MTE)[**P3**] measurement. In this thesis, the MQE is calculated with numerical integration. The $C_{\mathrm{V}}(T)$ in eqn. (39) is the heat capacity of the strand, *i. e.* the mixture of copper and Nb_3Sn. The heat capacity of Nb_3Sn is from [44, ch. 5.3], the properties of copper are from [49]. The critical temperature of Nb_3Sn is calculated from the ITER 2008 parametrization [50] which is used to define critical surface of the Nb_3Sn.

4 Quench heaters

After the meaning of disturbance spectrum was understood and the fact that the main reasons for degraded currents in magnets were mechanical and magnetic instabilities, it was necessary to ask [51, 52, 53] what is the level of perturbation the superconductors need to be stabilized against? To answer the question, *quench heaters* needed to be developed. Quench heaters are devices that can deposit a certain amount of heat in a superconducting strand, cable or magnet in order to initiate a quench. The history of quench heaters is long and many different techniques have been tried. The most natural way of implementing a quench heater is by using an electric heater element, *e. g.* embedded in a magnet. Thus it is not a surprise that indeed they were the first techniques that were used. Let us review two examples:

1. For comparing results to an MHD (Magneto Hydro Dynamic) generator magnet, wound with NbTi conductor, small test coils were produced [54]. Steel foils of 25 μm thick were embedded in the windings and used as a heater element. The heater energies were in the order of 0.1 J and the pulse widths in the order of 100 ms. The quench energies were increasing with respect to the pulse width. In the order of 10 ms the quench energy was independent of the pulse width. 2. In a project for enhancing the effectivity of propulsion in ships, the stability of a potted NbTi magnet was studied [55]. Straight heater elements consisting of bare constantan wire were embedded in the winding. Heat pulses shorter than 10 ms gave reproducible results with quench energies in the order of 1 mJ. These are examples of thermal stability of a magnet winding. Surely the heater energy is diffused to the superconductors, however also to the insulation, the mechanical structures and the heater itself, *i. e.* the superconductor is not the only variable with respect to the stability.

A few studies [56, 57] on stability were conducted with a bifilar magnanin coil consisting of 30 μm diameter magnanin wire wound around a NbTi multi filamentary superconducting strand. The heater element was 1 mm long and covered with epoxy in order to minimize heat leak to the helium bath around the strand. The width of the heat pulse was in the order of 10 μs and the quench energy was in the order of tens and hundreds of μJ. It was shown that the pulse widths shorter than 100 μs produced similar results. It is evident however, that the heat generated in the element is not all diffused to the wire. Some of the heat is diffused in the insulation and some stays in the heater element itself. It can be difficult to estimate the energy responsible for the quench.

Inductive heaters were introduced [58, 59] to tackle the problem of having to estimate the heater efficiency in case of the indirect heating. The inductive heater element

consisted of a bifilar coil around the superconducting strand. The coil was insulated from the strand by a silica tube which was in between the strand and the coil. The idea of this system is to generate an oscillating magnetic field which induces eddy currents at the surface of the sample. The eddy currents directly dissipate heat to the strand as they decay, thus it is easier to estimate the heat input to the strand when compared to the indirect electric heating method. The system works since the strands consist of superconducting filaments which are embedded in the stabilizer so the heat is dissipated in the crust of the strand where there are no superconducting filaments. However, the magnetic and the thermal time constants of the stabilizer are highly material dependent, and thus the system needs to be calibrated for different material parameters. Usually the stabilizer is made of copper, however different RRR (Resistivity Residual Ratio) values can have strong influence on the dissipated heat and pulse widths (eddy current decay time). Moreover the pulse needs to be fast enough to avoid magnetic disturbance in the superconducting filaments. Initially in [59] the pulses were generated with a heater element, however after problems with the thermal contacts and the time constants the heater was changed to the inductive system. Heated length of the wire was 3.5 mm and the oscillatory decay was typically 10 μs. The heating pulse lengths were in the order of 1 ms and thus for that study the adiabatic criterion was satisfied. In [58] with high purity copper and leads, decay time constants for the heating pulse of up to 300 μs were achieved. Similar technique was used also in [60] for studying the stability of NbTi strands for the LHC. A copper ferrule was used instead of the silica tube. The heat pulse time constant of 12 μs was achieved.

Interestingly, the indirect resistive heater element has been the most popular choice even after understanding the fundamental problem of the energy efficiency. For example, since the carbon paste heater was introduced [61] there have been several studies on strands and cables using this technology [62, 63, 64, 65, 66]. The heater element is made of highly resistive carbon paste which is put in between the sample and a copper strip. The strip acts as a current lead. A similar technique is used in the tip heater [67]. A conductive tip is used as a heater current lead instead of the copper strip. The tip heater is mainly intended for single strand measurements. More recently in [47] the possibility to use strain gauges as heating elements [68] was tested. They showed reasonable performance for cable stability standards, however the mechanical reliability was poor. The stability measurement was done in NbTi Rutherford cables in pressurized sample holder. The graphic paste heater technique was chosen for practical reasons, discarding the previously tested *Laser Quenching Technique* (LQT) [69]. Another problem with the

indirect heating is that the heater dissipates energy even after it is turned off since the element is still hot. The heater needs to be on until the quench and the absorbed energy is calculated by estimating it with a correction factor which depends on the pulse width. The factor varied between 0.4 and 0.95 as a function of transport current (heater duration variation), however only two regimes were introduced with correction factors of 0.9 and 0.6. For the sake of accuracy the estimation can be rather laborious. In [70] the thermal stability of Nb_3Sn Rutherford cables were studied by adopting the same technique and the estimation was done by introducing a transient 3-dimensional FEM thermal model.

A remarkable leap in the development of the energy deposition systems was taken when the LQT system was first introduced [71]. The system was built for studying the thermal stability of NbTi strands. The LQT is a fairly new technique for studying the stability of single strands [69, 71] and it is no doubt the most suitable technique for strand measurements due to its superior characteristics discussed in the work of [72]. These characteristics will be demonstrated later in the calibration measurements in this thesis. The technique has also been used for studying the thermal stability of a magnet [73]. The system in [72] consists of a single mode laser light source at room temperature, a silica-silica wave guide from room temperature to the cryostat and a sample holder for positioning the wave guide and holding the superconducting strand in place. A laser light pulse may be sent from the laser onto the strand. A part of the energy is absorbed as heat and part of it is reflected. Similarly to the inductive heating, this technique is a direct heating method. Although in first approximation (the light penetration into the strand is neglected), the energy is deposited onto the surface of the wire rather than inside it. In principle, the energy efficiency only depends on the absorptivity of the stabilizer. Moreover, only the thermal time constant of the composite superconductor itself controls the heat distribution in adiabatic assumption. One should notice that there is a great difference between the nature of thermal and magneto-thermal instabilities and thus their characterization require differently tuned LQT apparatuses. Obviously the apparatus introduced in [72] works well for its designed purpose. However, two details are needed to be optimized in this thesis: 1. the wavelength (807 nm [71]), it will be shown later that in order to maximize the absorptivity the wavelength needs to be close to the *plasma frequency* and 2. the pulse width (> 30 μs [69]). Reducing the pulse width is essential: the circular heated area on the strand in this thesis is 100 μm of diameter and the thermal diffusion time constant of the copper stabilizer in high RRR strands can be much shorter than 1 μs [13, ch 7]. In fact, the axisymmetric FEM model for round strands presented in [**P5**] was coupled with a thermal model. The model showed that

the self-field instability in a 0.8 mm RRP strand was not initiated when 1 μs and 2 μJ pulse was used, while it was quenching when the pulse width and pulse energy were reduced to 0.1 μs and 1 μJ, respectively. Therefore, for studying the MTI, one needs pulse widths shorter than 1 μs. A further complication is that the pulse should not be too short though, in order to avoid ablating the copper surface of the strand.

Q-switching technology can easily provide laser pulse widths in the order of 1 ns with energies in the order of 10 μJ/pulse. It is clear that the LQT can offer better performance than any of the earlier inventions. *All-silica* optical fibres are compelling choice for guiding the light on the sample surface. However, work is done to understand if the silica fibre can withstand such light intensities in deep *ultra violet* (UV, ≈ 110 nm) region which is *a priori* the most suitable wavelength with respect to the absorption of light; and to understand if the fibre is adaptable to cryogenic temperatures with such high light intensities [**P1**]. The other techniques fail to provide the fast energy deposition, moreover the indirect methods suffer from fundamental efficiency problems. The LQT is selected as the heating method in this thesis for studying the perturbation sensitivity of the MTI.

5 Metal optics

The deposition of heat energy in the LQT is done by heating the copper surface of the stabilizer. Hence, it is essential to ensure a good optical absorptivity. All metals comprise *free electrons*. The electrons are free to move in the conduction band of metals. Therefore, the behavior of the free electrons is dominant in metals when interaction with light is considered. Metal can be thought as a free electron gas, where electromagnetic waves can move inducing *plasma oscillations* or in other words, charge density oscillations [74, ch. 6.1.3]. Consider a cylindrical volume which is located in a uniform electron gas. If the electrons inside the volume are displaced in the direction of the axis of the volume, then a dipole moment is created corresponding to a polarization

$$P = -nex, \tag{43}$$

where n is the number of the electrons per unit volume, e is the elementary charge and x is the displacement. This is a source of an electric field which moves the electrons according to equation of motion [74]

$$m\frac{\mathrm{d}^2x}{\mathrm{d}t^2} = -\frac{ne^2}{\varepsilon_0}x. \tag{44}$$

The solution satisfies the electromagnetic wave equation, a harmonic at angular frequency

$$\omega_\mathrm{p} = \frac{ne^2}{\varepsilon_0 m}, \tag{45}$$

where ω_p is the plasma frequency. It is the natural oscillation frequency for a free electron gas, which means that it is the best frequency to ensure good absorptivity in metals. For most of the metals it is approximately at a corresponding wavelength of 110 nm. It has been shown in [75] that at 4.2 K the absorptivity of copper increases towards the ω_p, resulting 40% and 60% at wavelengths of 532 nm and 355 nm, respectively. Whereas the absorptivity of infrared (IR) wavelengths, including the 807 nm used in [69] is shown to be very poor [76], approximately 1%. The problem was solved by oxidizing the sample surface in order to increase the absorptivity to 22%. Given the facts above, it is evident that the easier way to cope with this problem is to use UV light. It should be noted that the light used for the energy deposition needs to be guided from room temperature onto the strand surface. In the following section optical fibres and their constraints to the experiment are considered. The relevant questions are: 1. How well the fibres can be mechanically adapted at cryogenic temperatures and to large temperature gradients? 2.

What are the dominant losses? And 3. what is the appropriate wavelength at cryogenic temperatures? In the next section the optical fibres are presented and their losses are discussed. The first and second questions were discussed also in [72] (however tested with different optical system).

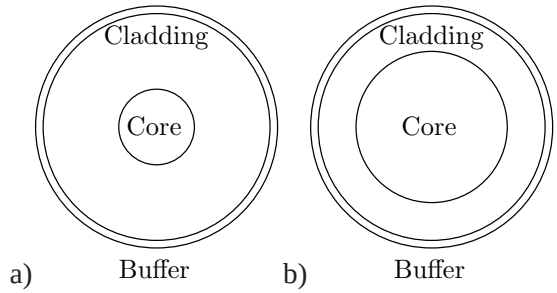

Figure 9. Geometry sketch of the multi-mode and single-mode optical fibres. a) SMF b) MMF.

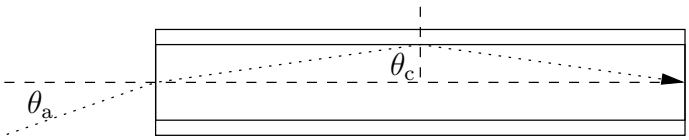

Figure 10. A sketch to calculate the acceptance angle for a step-index fibre.

6 Optical fibres

The optical fibre is usually made of a cylindrical dielectric wire. There are different structures in optical fibres: *single mode fibre* (SMF), *multi-mode step index fibre* (MMF) and *graded index fibre* (GRIN MMF) [77, ch. 9]. They consist of core, cladding and buffer (jacket) layers, which have different indices of refraction. It is required that the core has a higher index than the cladding in order to restrict the light via the total reflection from leaving the core. The geometrical difference between SMF and MMF is that the core is usually wider in the latter (figure 9) in order to accept more *modes* in the fibre. The modes are light beams accepted by the fibre with different reflection angles. The GRIN MMF are based on a gradual change of the refractive index in the core. The index gets smaller towards the edges of the fibre. Therefore, if the light has an angle between the central axis of the fibre, the path of the light is always curving towards the axis as it advances along the fibre.

Consider a light beam which arrives in a step index fibre with an angle θ_a (figure 10). The refractive indices are n_1 and n_2 for core and cladding, respectively. Assuming a *meridional ray* and that the fibre is surrounded by air the Snell's law yields

$$\sin\theta_a = n_1 \cos\theta_c = n_1\sqrt{1-\sin^2\theta_c}, \tag{46}$$

where θ_a is the acceptance angle which is the highest angle that is allowed for the

light beam to be guided by the fibre. Meridional ray means that the wave is confined to a meridional plane while *skew ray* follows a helical trajectory confined within two cylindrical cells with different radii [77, ch. 9]. The critical angle can be expressed in terms of indices of refraction which yields

$$\sin\theta_{\mathrm{a}} = \sqrt{n_1^2 - n_2^2} = \mathrm{NA}, \tag{47}$$

where NA is the *numerical aperture* [77, ch. 9.1]. For skew rays the acceptance angle is [78, ch. 2.2.4]

$$\sin\theta_{\mathrm{a}} \cos\gamma = \mathrm{NA}, \tag{48}$$

where γ is the angle between the core radius and the projection of the ray onto the fibre front face. The numerical aperture is a measure for the amount of light that is accepted in the fibre. However, not all the accepted angles are allowed, only the modes. They can be solved from the generalized Helmholtz equation for electro-magnetic waves (harmonics) [77, ch. 5.2]. The bound solutions for a fibre with core/cladding interface are found in [77, ch. 9.2], [79, ch. 4.8 and 6.6.1]. The important parameter achieved from the bound solutions

$$V = 2\pi \frac{a}{\lambda} \mathrm{NA} \tag{49}$$

is the *fibre parameter* [77, ch. 9.2], where a is the diameter of the core and λ is the wavelength. All the bound solutions need to satisfy the *field matching condition* [79, ch. 4.1]: the tangential field component must be continuous leading to *characteristic equation* [77, ch 9.2], [79, ch. 6.6.3] for *weakly guiding* step-index fibres

$$X \frac{J_{l\pm1}(X)}{J_l(X)} = \pm \frac{K_{l\pm1}(Y)}{K_l(Y)}, \tag{50}$$

which defines the acceptable modes. J_l are the Bessel functions of the first kind and K_l are the modified Bessel functions of the second kind, of the order l [80, p. 150],

$$X = a\sqrt{n_1^2 k^2 - \beta^2} \tag{51}$$

and

$$Y = a\sqrt{\beta^2 - n_2^2 k^2}, \tag{52}$$

where β is the propagation constant and $k = 2\pi/\lambda$. Weakly guiding means that the indices of refraction are almost the same in the core and in the cladding ($n_1 \approx n_2$). For each azimuthal index l the equation has multiple solutions corresponding to multiple propagation constants. Therefore the propagation is discretized β_{lm}, where each $m = 1, 2...$ represents a mode [77, ch. 9.2]. The guided modes are referred as "LP$_{lm}$

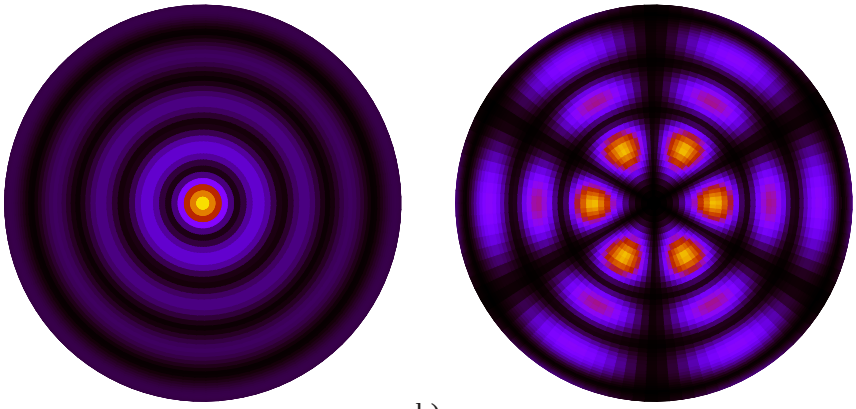

a) b)

Figure 11. Graphical representation of the intensity of different modes in a fibre. a) LP_{01} and b) LP_{35}.

modes" [79, ch. 4.6 and 6.6.1]. For example LP_{01} is a meridional ray which has TE or TM polarization and LP_{35} is a skewed ray which has H or E polarization (figure 11). When the fibre parameter gets higher, the characteristic equation has more solutions [77, ch 9.2], [79, ch. 6.6.3]. The exact number of solutions depending on the fibre parameter can be approximated when $V \gg 1$ [77, ch. 9.2]

$$M \approx \frac{4}{\pi} V^2, , \tag{53}$$

while the *single-mode condition* is

$$V < 2.405. \tag{54}$$

In single-mode the fibre is able to guide only one mode.

The equations (49) and (53) show that the number of modes in weakly guiding round optical step-index fibres is dependent on the wavelength of the guided light, radius of the core and the numerical aperture. Therefore, the core diameter is usually smaller in the single-mode fibres than in multi-mode fibres.

6.1 The dominant losses in optical fibres

The guided light interacts with the dielectric medium that is used in optical fibres. The light is attenuated via the fundamental scattering processes, absorption and scattering due to inhomogeneities created in the fabrication process [81, ch. 10.4]. The attenuation is expressed with Lambert's law as follows

$$-\frac{\mathrm{d}I}{\mathrm{d}z} = \alpha I, \tag{55}$$

where I is the intensity, z is the direction of the wave propagation and α is the transmission loss coefficient, which is generally expressed as [82, p. 684]

$$\alpha(\lambda) = \frac{A}{\lambda^4} + B + C(\lambda), \tag{56}$$

where A is the Rayleigh scattering coefficient, B is the loss induced by structural imperfection and $C(\lambda)$ is the wavelength-dependent loss induced by impurities and intrinsic absorption. One of the fundamental losses in glass is the Rayleigh scattering. The scattering is proportional to the λ^{-4}. Therefore, the losses due to the Rayleigh scattering are increased if the wavelength is reduced for example from 807 nm to 355 nm. The behavior is explained by the Mie's theory, which describes the absorption and scattering of light by small spheres [83, ch. 5]. It is due to the microscopic fluctuation of the density or the composition in glass. The structural imperfection induced broad band loss can be caused, for example, by longitudinal fluctuation of the core-cladding interface. The fluctuation may be due to *micro bending*, which can take place at cold temperatures [84, ch. 6]. If a fibre is bent, certain modes can be lost due to *macro bending* [84, ch. 6]. It is shown in [**P1**] that micro bending in 100 μm core all-silica polyimide buffered optical fibres (FVP100110125) is relevant at cryogenic temperatures. The loss can be 25% (1.2 dB) at 355 nm when the length of the fibre is 3.5 m. A macro bending test was conducted for the same fibre at room temperature. A loop of 20 mm of diameter did not show any significant loss at 355 nm. Only the 100 nm core fibre was tested. It should be noted, that the macro bending is more severe issue if the diameter of the fibre is increased or the bending radius is reduced [84, ch. 6][85].

For silica, the only fundamental losses are Rayleigh scattering and absorption via the Si-O bond vibration. The Si-O bond vibration causes a very strong wavelength-dependent loss at infrared wavelengths (> 1.55 μm). Other possible losses are the wavelength-dependent losses which arise from hydroxyl bonds and the transition metal impurities. [82, p. 684]

Multiphoton photoluminescence can occur in a medium, when two or more photons $k \geq 2$, with the same energy hf_1 together have enough energy khf_1 to excite electrons to higher energy levels. The excited electrons spontaneously decay to a lower energy level emitting single photons $hf_2 \geq hf_1$ resulting fluorescence light [77, ch. 13.5]. A process were two or more electrons are absorbed is called the *multiphoton absorption*, moreover a process where the fluorescence light is emitted after is called the *multipho-*

ton photoluminescence. The probability of having k electrons at the same place and time, determined by the uncertainty principle [86, ch. 9.7], is equal to the probability of observing one electron at given place and time to the power of k. Therefore, the probability for a multiphoton absorption is proportional to the intensity of the incident light, $I^k(r,t)$. The attenuation in a material where the two photon absorption takes place is defined as [86, ch. 9.7]

$$-\frac{\mathrm{d}I}{\mathrm{d}z} = \alpha I + \beta I^2, \tag{57}$$

where

$$\beta(\omega) = \frac{2\hbar\omega}{I^2} W_{\mathrm{T}}^{(2)}(\omega) \tag{58}$$

is the two photon absorption coefficient, ω is the angular frequency and $W_{\mathrm{T}}^{(2)}(\omega)$ is the transition rate between two bands. It can be seen that at high intensities the two photon absorption becomes an issue. In our case this can be relevant since the pulse width is in the order of 1 ns and the fibre is only 100 μm of diameter which makes the peak intensity high.

6.2 Fluorine doped high OH-content all-silica fibres

The most used dielectric material in optical fibres is silicondioxide (silica, SiO_2). When it is used for both, core and cladding, the fibre is called *all-silica fibre*. Silica can be doped with different impurities in order to reduce the index of refraction. One of the possible dopants is fluorine, providing indices 1.46941 and 1.46485 at 365 nm wavelength for 1 % and 2 % F-doped (fluorine doped) silica glass, respectively, while in pure silica the index of refraction is 1.47486 [87]. By using 1 % or 2 % F-doped silica cladding and pure silica core, a weakly guiding fibre may be fabricated whose numerical aperture at 365 nm is 0.127 or 0.172, respectively. The numerical aperture can be further increased by adding more F-dopant. The fluorine doped silica fibres show excellent transmission properties in UV-light region and are therefore widely used in UV-applications [88, 89][**P3**].

In pure silica there are defects which affect negatively on the transmission. The best known defects are the three E'-center variants [90]. The so called *generic* E'*-center* consists of an unpaired electron in sp^3 orbital in the Si atom which is bonded to only three oxygen atoms. It is denoted with $\equiv\mathrm{Si}\bullet$ (also $\mathrm{Si}^{\bullet}$), where the dot corresponds to the unpaired electron and the three lines to the Si bonds. The hyperfine structure of the sp^3 orbital of the E' (variants E'_α, E'_β and E'_γ) is distinguishable in electron spin resonance (ESR) spectrum. Their population is temperature dependent (different for each variant).

This is because the recombination of the broken bonds depends on the movement of the mobile hydrogen atoms, which depends on the temperature [90, 91].

The E'-center creation mechanism requires activation energy, which can be provided via irradiation. For example UV-light can break the $Si-O-Si$ bonds into *non-bridging oxygen hole centers* (NBOHC, $\cdot O-Si\equiv$, also $Si-O^{\circ}$) and E'-centers ($Si^{\bullet}$). The absorption bands for E'-centers and NBOH-centers are at 214 nm (5.8 eV) and 265 nm (4.7 eV), respectively [92]. In all-silica fibres the dominant nonlinear attenuation mechanism is the two photon absorption which is dependent on the intensity and the length of the fibre [93, 94]. In all-silica fibres the two photon absorption is expected at wavelengths lower than 330 nm with high intensities $>$10 MW/cm^2 and fibres lengths $\geq$3.5 m [95] leading to irradiation induced damages. The high OH content (1200 ppm) in fused silica glass has a natural protection mechanism against high energy irradiation [91], the OH molecule can heal the broken bonds. Moreover, *Hydrogen loading* can be used to heal irradiation induced damages in silica as shown in deep UV-region below 330 nm wavelengths, after irradiation with deuterium lamps [96], with pulsed excimer-laser or 4$^{\text{th}}$ harmonic Nd-YAG lasers [97] and with Gamma-sources [98]. The mobile hydrogen molecules are able to move in the glass and they transform the broken molecules to $Si-OH+H-Si$ [92].

Given these facts, it is compelling to build the LQT apparatus with fluorine doped high OH-content all-silica fibres coupled with a Q-switched laser providing 355 nm light. However, it is questionable if the degradation and healing mechanisms of silica described above are similar at cryogenic temperatures than at room temperature. In [**P1**] it was shown that the two photon absorption is still an issue for the fibres with wavelengths under 330 nm at 4.2 K. For the testing a 355 nm Q-switched laser with 70 μJ pulse energy, 1 ns pulse width and 100 Hz repetition rate was used. Moreover tests for hydrogen loaded and unloaded fibres were conducted with deuterium lamp irradiation and a 355 nm Q-switched laser with 1 μJ pulse energy and 25 kHz repetition rate. The hydrogen healing did not not vanish even though it was thought that the mobility of the hydrogen atoms could be slower due to the cryogenic temperature and thus hinder the healing process. In fact the hydrogen loaded fibres didn't show any irradiation induced degradation during 12 hours of laser irradiation (1080 million pulses) or 6 hours of deuterium lamp irradiation and in [**P2**] it was shown that the irradiation induced damages are reduced at boiling nitrogen temperature compared to room temperature. The problem with hydrogen loading is that hydrogen diffuses out from the loaded fibres if they are kept at room temperature for a long period of time [99, 100]. To prevent this the

fibre need to be kept in relatively cold temperatures (-18°C).

After deep consideration of several different design aspects of the MTI apparatus, it was decided to use the 100 μm core all-silica polyimide buffered optical fibre (FVP100110125) as a wave guide from the laser light source at room temperature onto the strand surface at cryogenic temperatures keeping in mind that the wavelength should be higher than 330 nm.

7 Lasers

Lasers are optical resonators. The oscillation in the optical resonator is normally initiated by an existing input signal. The signal is amplified and fed back to the input of the resonator with a matching phase, which is further amplified by the resonator. This process continues until the gain of the resonator is saturated; the laser reaches a steady state with large output signal. The optical resonator is built by using one mirror and one partially transmitting mirror which are perpendicular to the beam and facing each other. The light is reflected back and forth between the mirrors. In the middle of the two mirrors there is an active medium which amplifies the light. [77, ch. 15]

In the laser, the active medium is the amplifier. The amplification is based on the stimulated emission of radiation: the higher energy levels of the active medium is populated via pumping. When photons stimulate the electrons in the higher levels, the pumped energy is emitted by the electron transition to the lower states. The amplification is described with the differential rate equations of the population densities [77, ch. 14.2]. The active medium cannot maintain a fixed gain in case of high powers, it would require an arbitrarily high energy pumping. Therefore, the basic property of the active medium is gain saturation.

7.1 Q-switching

In the MTI apparatus, a high intensity pulsed light is needed. A continuous wave (CW) laser might be used as a pulsed laser by using a switch or modulator to restrict the transmission at times when the light is not needed. However, this technique does not conserve the energy at the times when light is not needed and thus peak energies above CW light are not possible. Therefore, it is not recommended to use modulated CW light as a pulsed source. There are several natural techniques to generate pulsed light with lasers: gain switching, Q-switching, cavity dumping and mode locking [77, ch. 15.4].

In Q-switching the output of the resonator is periodically restricted (on/off). It is done by changing the quality factor (Q-value) of the resonator. It can be done with a modulated absorber which is inside the resonator to prevent the light from oscillating inside it. The level of pumping is kept constant all the time. Therefore, during the restricted output, the population of high energy level in the active medium increases: the energy is stored. When the oscillation process is restored, the accumulated energy is released in an intense and short pulse of light. The rate equation for the photon number density is [77, ch. 15.4]

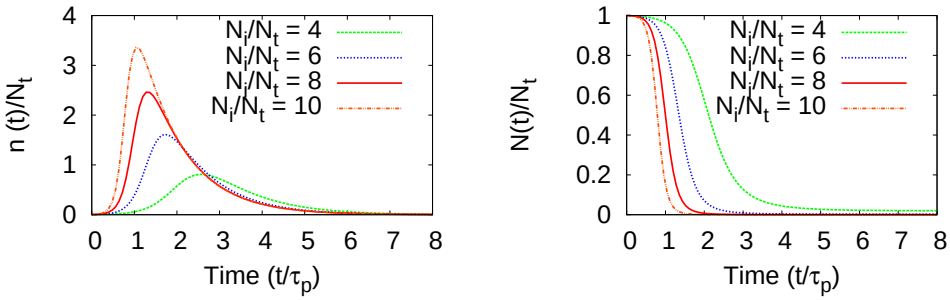

a) b)

Figure 12. Example of a typical Q-switched laser. a) pulse shapes and b) population differences evolution calculated by numerical integration. The time is normalized with the photon life time τ_p. The photon number and population difference is normalized with the threshold population difference N_t.

$$\frac{\mathrm{d}n}{\mathrm{d}t} = \left(\frac{N}{N_\mathrm{t}} - 1\right)\frac{n}{\tau_\mathrm{p}} \tag{59}$$

and

$$\frac{\mathrm{d}N}{\mathrm{d}t} = -2\frac{N}{N_\mathrm{t}}\frac{n}{\tau_\mathrm{p}}, \tag{60}$$

where n is the photon number density, N is the population difference, N_t is the population difference threshold and τ_p is the photon lifetime. The differential equations show that the pulse duration shortens and the peak energy of the pulse increases when the threshold population difference decreases. An example is shown in figure 12.

7.2 Neodymium-doped yttrium aluminum garnet

There are different pumping schemes for lasers depending on what kind of active medium is used. So far the most commonly used crystal in solid-state lasers is the Neodymium-Doped Yttrium Aluminum Garnet (Nd^{+3}:YAG, Nd-YAG) [101, ch. 2.3.1]. It has high gain and low population difference threshold, which is optimal for Q-switching (high peak power, see figure 12). In addition to the favorable lasing characteristics, it has desirable physical, mechanical and chemical properties. The YAG host is hard and stable from low temperatures up to its melting temperature, no transformations are reported in the solid state and it has a high thermal conductivity [101, ch. 2.3.1].

For Nd-YAG, developed in the 1960s, the most common laser line is offered at 1064 nm, which is the strongest fluorescence output [101, ch. 2.3.1], [77, 15.3], [102]. The

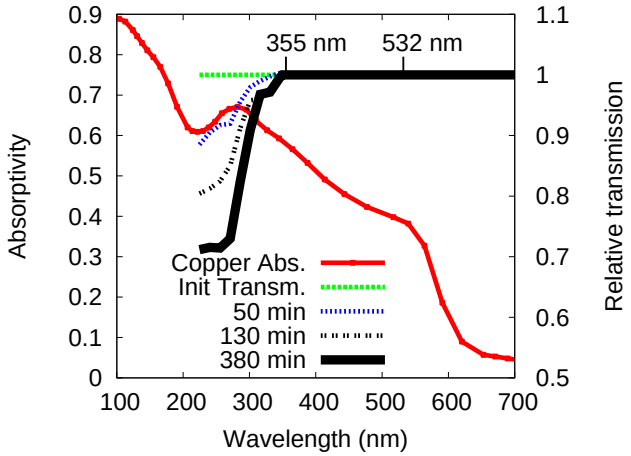

Figure 13. Relevant design attributes of the optic system: absorptivity of copper at 4.2 K [75] and relative transmission in the all-silica fibre as a function of wavelength [**P1**]. The transmission is relative to the initial transmission and it is shown in different times of the irradiation treatment. The chosen laser lines at 355 nm and 532 nm are shown in the figure.

Nd-YAG may be diode pumped at 808 nm wavelength which is effectively absorbed via transition from ground level $^4\mathrm{I}_{9/2}$ to the level $^4\mathrm{F}_{5/2}$ [101, ch. 2.3.1]. The 1064 nm laser line is generated by the transition from $^4\mathrm{F}_{3/2}$ manifold at 1.4269 eV to the $^4\mathrm{I}_{11/2}$ manifold at 0.2616 eV [101, ch. 2.3.1], [77, 15.3]. The frequency can be doubled by *second harmonic generation* (SHG) and further tripled by *sum-frequency generation* (SFG) [77, ch. 21.1]. The generated laser lines are then at 532 nm and 355 nm respectively.

Figure 13 shows a summary of the relevant design attributes of the optic system. The transmission through the fibre degrades with respect to time below 330 nm due to the irradiation damages explained in the previous section. On the other hand the absorptivity decreases if the wavelength is increased. Thus, a compromise is needed. A diode pumped passively Q-switched Nd-YAG laser with 2$^{\mathrm{nd}}$ (532 nm, green) and 3$^{\mathrm{rd}}$ harmonic (355 nm, UV) lines was chosen for the MTI apparatus. The lines can be seen in the figure, too. The nominal pulse energy of the laser is 70 μJ/pulse with 1 ns pulse width and up to 1 kHz repetition rate. It is also equipped with a *single shot* option mode, which allows the user to trigger the laser once at a given time. The single shot is essential for the MTI measurement where only one pulse is given.

Table 4. Characteristics of the laser.

Characteristics	
Pulse energy	70 μJ
Attenuation	2%-100%
Pulse width	$\approx$ 1 ns
Wavelengths	355 nm, 532 nm
Repetition rates	1 Hz-100 Hz, 1 kHz
External trigger	Single shot mode
Coupling	Integrated (SMA-connection)

8 The LQT apparatus

8.1 Calibration

After the use of LQT for studying the perturbation sensitivity of the MTI was theoretically justified, it was necessary to calibrate the relevant energy associated with the quench. In [72] is reported the laser calibration that was done in a vacuum chamber at 4.2 K. The calibration was conducted with two types of experiments: 1. Transmission experiment and 2. Absorptivity experiment. Thus the following characteristics were defined: the total energy guided by the fibre in the first phase and the energy absorbed by the copper in the second phase. The power was measured with a bolometer which consisted of a light absorber connected to a thermal drain. The thermal conductivity of the drain was estimated, by measuring the electric resistivity of it and applying the *Wiedermann-Franz law*.

For this thesis [**P3**] it was considered more reliable to calibrate the power against a known heater. First a copper piece was heated up with the heater at several power levels and then the heating up was repeated with the laser as power source. From the difference of the heater and laser power-temperature curves a loss factor can be calculated which in the first phase is the cryogenic loss and in the second phase it is the absorptivity. The chosen optical components of the LQT apparatus are: 1. Q-switched pulsed Nd-YAG laser with 2^{nd} and 3^{rd} harmonics and an integrated coupler (table 4), 2. polyimide buffered high OH-content all-silica MMF fibre which is coupled to the laser with an SMA-connector. The characteristics of the fibre are in table 5. According to the table the fibre has plenty of modes, which makes the optical output extremely uniform. In case of an uneven distribution the energy of the pulse cannot be as elevated as in uniform distribution since the damage threshold of the metal might be exceeded at some hot

Table 5. Characteristics of the fibre [103].

Characteristics	
Product descriptor	FVP100110125
Core material	Silica, high OH (without hydrogen)
Core diameter	100 μm
Buffer material	Polyimide
Buffer diameter	125 μm
Cladding diameter	110 μm
Cladding material	Silica, F-doped
Numerical aperture	0.22 ± 0.02
Acceptance angle	12.7°
Modes at 355 nm	193 000, eqn. (53)
Modes at 532 nm	86 000, eqn. (53)
For 10 m long fibre, transmission	from 220 nm up to 1200 nm

spots, which would be the case in single mode fibre used in [72] (figure 11). However, the average intensity of the light in [72] with 1.2 W and 300 μm diameter optical tip was in the order of 2 kW/cm^2 which should not be an issue. While in this case with 100 μm core fibre the intensity may get up to 0.4 GW/cm^2 which is close to the threshold limit for copper [104].

8.1.1 Setup

The fibre was used to guide laser pulses from room temperature into a vacuum chamber at 4.2 K in a cryostat, see figure 14 a. Outside of the cryostat, the fibre was coupled with the laser whose energy could be monitored with a photo detector, placed before the coupler. 50 cm of the fibre from the connector was outside of the cryostat and protected with a heat shrink tube until the inside of the cryostat. The feed through from room temperature into the cryostat was fixed with Araldit. Inside the cryostat the fibre was unprotected. The feed through from the cryostat into the vacuum chamber was made of a stainless steel pipe filled with Stycast glue. The chamber was immersed in liquid helium bath at atmospheric pressure. The level of the liquid helium was varying between 400 mm and 1000 mm during the measurements because the cryostat was filled once a day and the level was not regulated. However, the chamber was always submersed in the helium bath. Inside the chamber, there was a copper mass which was anchored

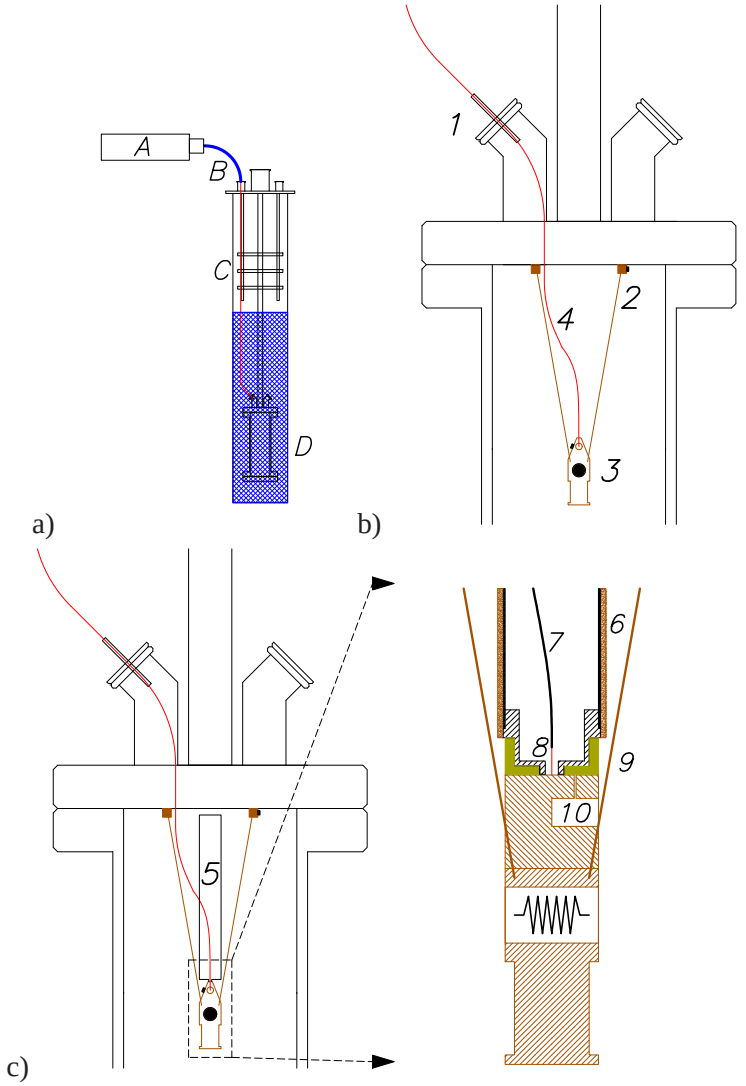

Figure 14. The sketch of the calibration setup: a) *A* is the laser, *B* is the optical fibre, C is the radiation shielding and *D* is the vacuum chamber inside the cryostat. b) *1* is the vacuum feed through; *2* is the thermal grounding via copper wires which are attached on the wall of the vacuum chamber by using a copper ferrule (the black rectangle is a temperature sensor); *3* is the copper mass with the heater (black circle), the temperature sensor (black rectangle) and the black body cavity (brown open circle); *4* is the unprotected optical fibre. c) 5 is the reflection screen. The head of it is represented in detail with the copper mass on the right hand side; 6 is the copper braid, 7 is the stainless steel tube, 8 is the fibre inside the tube, 9 is the Ultem 2100 cap between the screen and the copper mass; 10 is the black body cavity.

(which will be called also grounding, because of the analogy with electric circuit that is used) to the walls of the chamber via four 1 mm diameter and 30 cm long copper wires, see figure 14 b. There was a cavity in the copper mass which was acting as a black body [86, ch. 10.4], where all the light was guided by using the fibre in the first phase of the experiment. The fibre was fed in the black body cavity through a 150 μm hole in the copper mass. The end face of the fibre was set up in the middle of the cavity. In the second phase, the fibre was put on top of the copper mass in order to let the light reflect from the surface. A thermally grounded reflection screen which was insulated from the copper mass was put around the reflection point to absorb the reflected light, see figure 14 c. The reflection screen is a well polished stainless steel tube where the light reflects until it is completely absorbed. At room temperature, the optical reflectivity of stainless steel is in the order of 50% and 60% for 355 nm and 532 nm lights [105]. The reflectivity should not change drastically at cryogenic temperatures. For example in pure iron it doesn't show noticeable difference between room temperature and 4.2 K [75]. Thus after 10 reflections the intensity is less than 0.1% of the initial value. The fibre was fed in the reflection screen through a tiny stainless steel tube which guided the end face of the fibre on top of the copper mass. The thermal grounding was made with a copper braid soldered on the reflection screen and the insulation was made with Ultem 2100 cap between the copper mass and the screen. Cernox temperature sensors were installed on the copper mass and on one of its grounding point. The Cernoxes were driven by a 10 μA current source and the voltage was measured with a Keithley 2000 Multimeter. A heater of 100 Ω was installed in the copper mass. The heater was driven with a Keithley 2410 current supply with precise current measurement. The heater voltage was measured with a Keithley 2000 Multimeter.

8.1.2 Measurement data

During the test five values were monitored: 1. thermal ground temperature, 2. copper mass temperature, 3. heater power, 4. laser power and 5. the helium level. Figure 15 represents examples of the heater and laser measurements. The figure show that the time constant of the system is much higher when the heater is used compared to the time constant of the laser heated system. Let us consider the thermal circuit of the calibration experiment (figure 16). The thermal time constant of an RC circuit is $\tau = RC$, where R is the thermal resistance and C is the thermal capacity. Now, the $R_{\mathrm{h}} \gg R_{\mathrm{w}}$ due the low thermal conductivity of the heater which consists of bifilar constantan coil covered with epoxy. Thus the R_{h}, C_{h} and P_{h} can be approximated with a current driven parallel

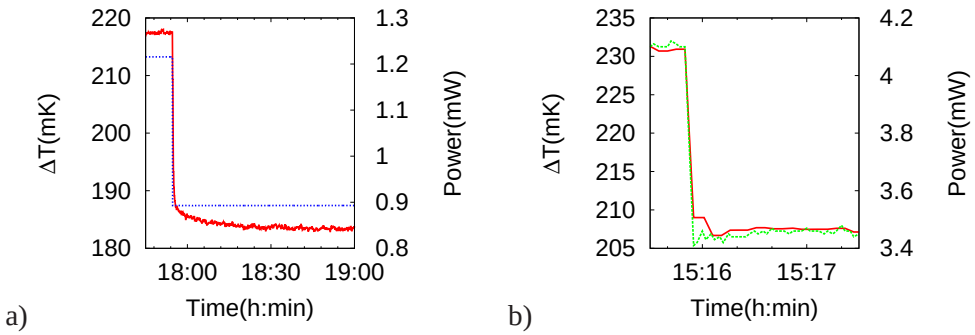

Figure 15. Examples of the measurements a) Heater power (····) and ΔT between the copper mass and the thermal ground (—). The time constant of the system is high due to the heater's low thermal conductivity. It took one hour to reach the stable condition. b) Laser power (····) and ΔT between the copper mass and the thermal ground (—). The stable condition was reached in seconds because the laser heated the copper, which has a high thermal conductivity, directly.

RC circuit (with a thermal time constant $\tau_{\mathrm{h}} = R_{\mathrm{h}}C_{\mathrm{h}}$). On the otherhand, when the laser is used: R_{w}, C_{c} and P_{l} can be approximated with similar circuit (with $\tau_{\mathrm{l}} = R_{\mathrm{w}}C_{\mathrm{c}}$). Thus, since $R_{\mathrm{h}} \gg R_{\mathrm{w}}$, the time constant of the heater is much higher than the time constant of the laser which directly heats the copper. This experiment demonstrates the fundamental problem of indirect heating and particularly the problem of the electric heater. An electric heater must be electrically resistive and at the same time thermally conductive. For example in metals this is impossible according to the *Wiedermann-Franz law*. This problem was understood and solved with remarkable idea of the LQT system in [72].

In order to test the effect of environment on the system, a measurement was conducted where three environmental perturbations were given to the system. The perturbation types are: 1. Helium transfer, 2. Reconnection of the SMA-connector and 3. Hot air (62 °C) to the fibre coupler. The measurements are shown in figure 17. The figure shows that the environmental perturbations do play a role. In order to analyze the behavior of the system it should be noted that the laser heated mass, that is the copper, is fast enough to follow the changes of the ground temperature and the ground is not completely independent of the copper mass temperature as shown in figure 18. Therefore, if the laser heating power changes, the ΔT and the thermal ground should both change and have proportional behavior. The perturbations in the laser measurement and the effect of helium transfer on ΔT in heater measurement are shown in figure 19. The figure

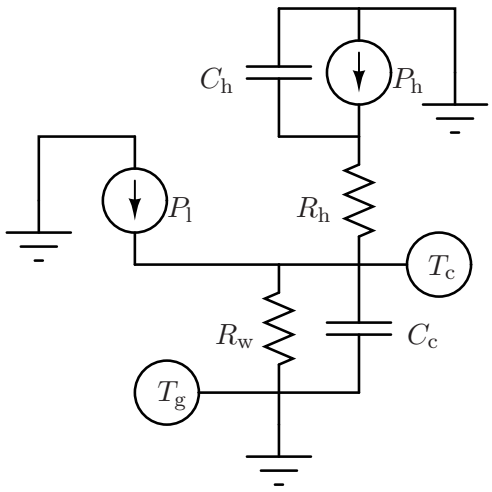

Figure 16. Thermal circuit schematic of the calibration experiment. P_l and P_h are the laser and the heater power inputs, respectively. R_h is the thermal resistance from the heater to the copper mass, C_h is the thermal capacity of the heater and R_w is the thermal resistance from the copper mass to the walls of the vacuum chamber. C_c is the heat capacity of the copper mass. T_c and T_g are the temperatures of the copper mass and the thermal ground, respectively.

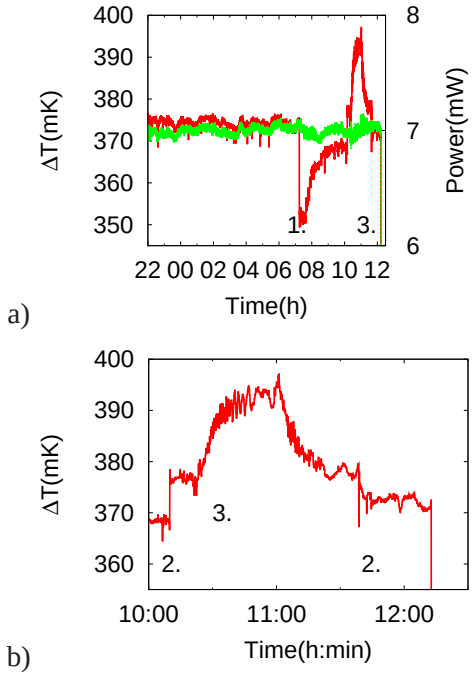

Figure 17. Example of the perturbation measurements, where three environmental perturbations were created: 1. Helium transfer, 2. Reconnection of the SMA-connector and 3. Hot air (62 °C) to the fibre coupler. The ΔT (—) is approximately 375 mK at first, however ends up being 370 mK. a) The whole measurement is showed, with the perturbations 1 and 3, where the laser power is represented by (·····) b) Detailed figure showing the measurement from 10:00 to 12:30: perturbations 2 and 3 are shown with better accuracy.

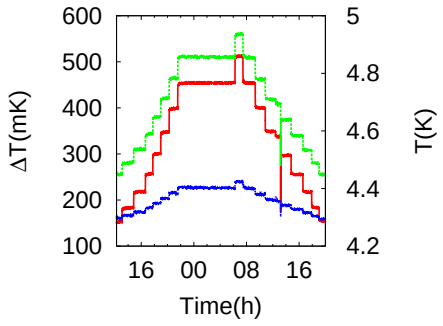

Figure 18. Example of the heater measurements. The ground temperature (····) follows the mass temperature (·····). The ΔT (—) is the difference of the two.

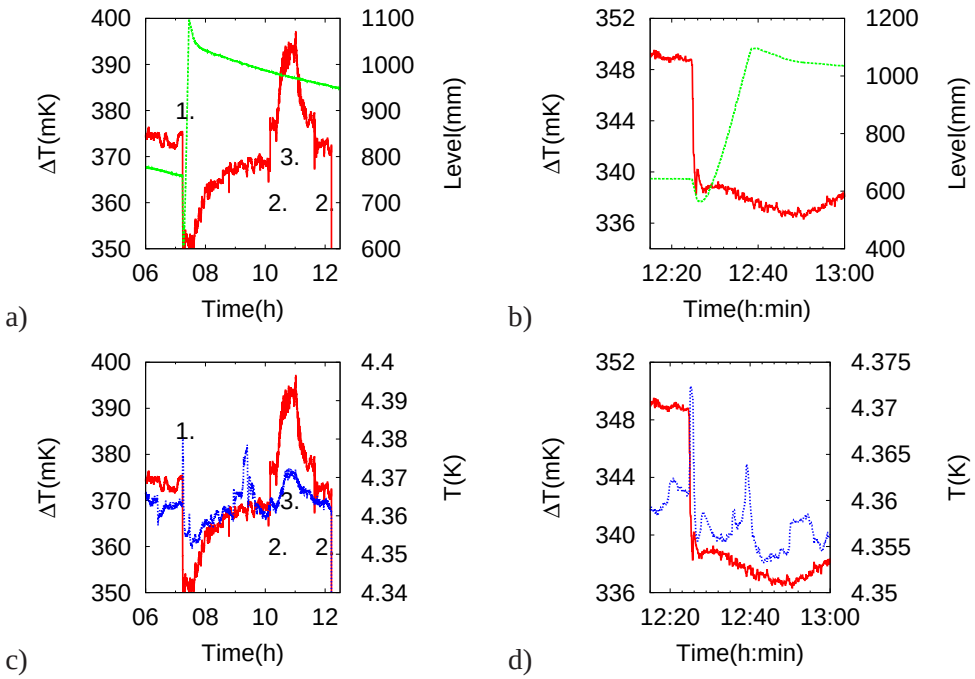

Figure 19. a) The effects of the environmental perturbations on ΔT (—) while measuring with laser. The helium level is represented by (·····). b) The effect of helium transfer on ΔT while measuring with heater. c) and d) are the same as a) and b) except for the right hand side y-axis is changed from the helium level to temperature of the thermal ground (····).

shows that the helium transfer plays a role also in the heater measurement. The reason could be that during the helium transfer the four mounting points have different temperatures. As only one of the points is measured, the ΔT would have a shift. In this case, the shift would be transient as it seems to be in figure 19 a. During the helium transfer there is not a clear indication of micro bending in the fibre which could be generated by the temperature variation in the cryostat (see section 6.1). Surely, there is a shift in the ΔT however in both, laser and heater measurements. The magnitude is in the order of 10 mK for both and thus it is difficult to draw conclusions of the micro bending. In figure 19 c the perturbation 1 affects both temperatures, which means that the laser heating power changes. Similarly the laser power changes for the 2. and 3. perturbations. In the figure between 9:00 and 10:00 there is a spike in the thermal ground's temperature, which is not seen in the ΔT, which means that it was a thermal perturbation, not due to the laser. These peaks are seen also in the figure 19 d and again they are not followed by the ΔT.

The perturbation 2 which is the reconnection of the SMA-connector clearly had an effect on the transmission of the light. It is due to the changing optical coupling between the laser and the fibre. Therefore, it is essential that the SMA-connector is always connected in the same angular orientation. The perturbation 3 shows that the fibre coupling is not thermally stable. It is therefore important to have stable environmental conditions for the laser. However, the air was 40 °C higher than room temperature and the effect on ΔT was only 15 mK.

The photo detector inside the laser was calibrated with an Energy meter, EnergyMax from Coherent. The results are shown in figure 20. The fitting curve for the photo detector at 100 Hz calibration is a straight line. The energy of the laser beam is partly lost due to coupling loss, micro- and macro bending. Most of the losses originates from the coupling. In theory the highest possible coupling efficiency is approximately 90%. However, in the case of small fibre diameter the efficiency is smaller. The measured transmission through the fibre at 355 nm was 35% where the loss is mainly due to the coupling. This loss could be reduced by choosing a bigger fibre diameter. However the macro bending losses would increase and opto-mechanical properties would have to be tested. The coupling changes with respect to the state of the end and front faces of the fibre and thus it needs to be checked prior to every measurement. In case the transmission was lower than 35%, the fibre end face was polished. The front face was well protected and thus it never needed to be polished. With 532 nm the transmission changed linearly between 26% and 32% with respect to pulse energy which is due to the changing opti-

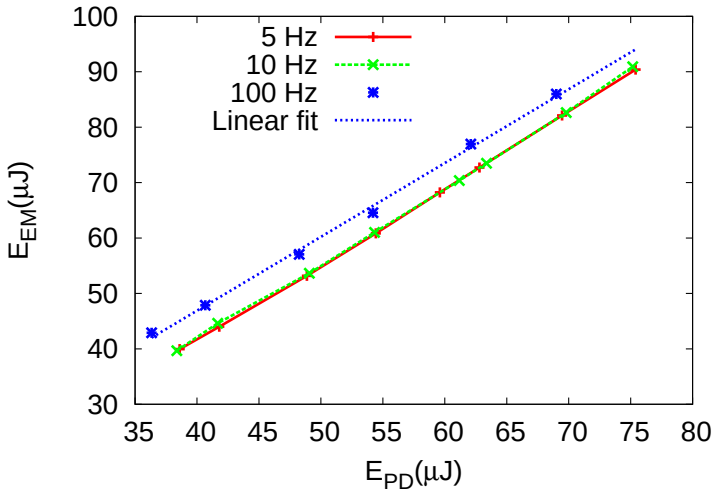

Figure 20. An example of the photo detector calibration curves at 355 nm. The repetition rates are 5 Hz and 10 Hz and 100 Hz. Only 100 Hz is fitted with a straight line since it is used for the cryogenic calibration. E_{PD} and E_{EM} are the energies of the photo diode in the laser and the energy meter, respectively.

cal output of the laser. It is notable that the energy meter has an active circular area of 10 mm of diameter and the end face of the fibre should not be in touch with the surface of the active area in order to avoid irradiation damage. Thus, if light is scattered from the end face of the fibre, it is not counted in the energy measurement. While, if the same scattering takes place in the cavity the scattered light contributes to the temperature. Therefore the value at room temperature could be slightly lower than in reality.

8.1.3 Analysis

The analysis of the measurements in [**P3**] was done as follows. The heater calibration curve

$$\Delta T = \Delta T_{\mathrm{h}}(P_{\mathrm{h}}) \tag{61}$$

at 4.2 K is shown in figure 21. The figure shows that the calibration was reproducible throughout the measurements even after *Hydro-Thermic Cycle* (HTC) and *Thermic Cycle* (TC). In HTC the system was warmed up to room temperature and the vacuum chamber was filled with nitrogen gas. Then the vacuum was re-pumped and the system was cooled down again to 4.2 K. In TC the system was warmed up and cooled down without breaking the vacuum in the chamber.

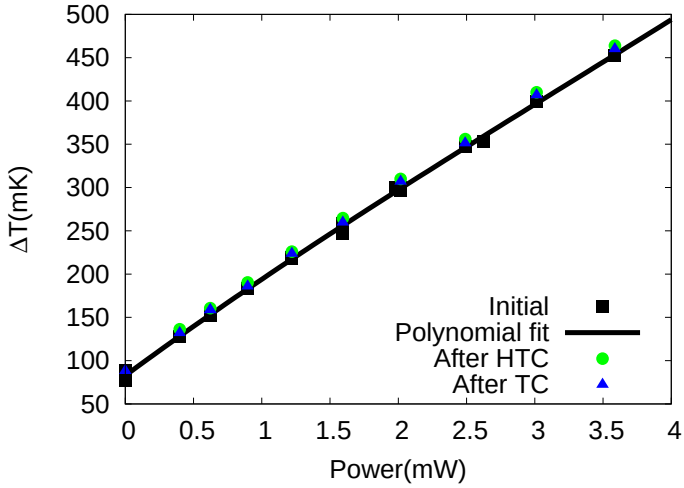

Figure 21. Heater calibration curve and 2 verification measurements.

The beam power of the laser was measured at 4.2 K in the copper mass with 100 Hz repetition rate at 355 nm and 532 nm wavelengths with different laser output powers. The results provided similar curves

$$\Delta T = \Delta T_{\mathrm{l}}(P_{\mathrm{l}}) \tag{62}$$

as for the heater calibration curve in equation (61). The loss factor η could now be found with

$$\min \sum_{P \in \mathbf{P}_{\mathrm{h}}} \left[\Delta T_{\mathrm{h}}(P) - \Delta T_{\mathrm{l}}((1-\eta)P)\right]^2, \tag{63}$$

where $\mathbf{P}_{\mathrm{h}}$ is the discrete measurement range for the heater. In the first phase of the experiment the loss factor represents the cryogenic loss and in the second phase it represents the optical reflectivity of the copper.

The cryogenic transmission loss should be 13% for 355 nm light in this case according to earlier tests [**P1**]. The cryogenic loss of the fibre was only 5.5% and 1.8% at 355 nm and 532 nm, respectively [**P3**]. In the earlier case, the measurement was done for a fibre which was more than two times longer and looped 4 times (10 mm bending radius) in liquid helium, therefore a higher cryogenic loss is possible. Also the cryogenic loss was measured with a deuterium lamp which has a wide spectrum in deep UV-region with different power output than the laser.

As already explained in section 5, the absorptivity of copper should increase towards the plasma frequency, and should be in this case 40% and 60% at 532 nm and 355 nm,

respectively (see also figure 13 in section 7). The corresponding values observed in the calibration experiment were 89% and 83%. The difference might be due to different surface properties or back reflection from the screen. However the reflection screen was well polished and the possibility to reflect back to the copper surface was minimized by making the hole around the reflection point very small compared to the screen, see figure 16 c.

It has been reported that at room temperature high intensity light (average peak power in this case being ≈ 0.4 GW/cm^2) might change the surface properties of copper [104]. Moreover, the reflectivity of an irradiated metal surface decreases significantly due to the high intensity of laser pulses [106]. For copper, high intensity 532 nm light seems to be slightly more efficient than 355 nm. It has been shown in [104] that 532 nm outperforms 355 nm light in etching copper foils due to the nature of the plasma formed above the surface of the material. The high absorptivity is noteworthy, since the earlier studies with IR light in [72] required black coating on the strand in order to have 22% absorptivity, while here the coating is not needed and the absorptivity is almost four times higher.

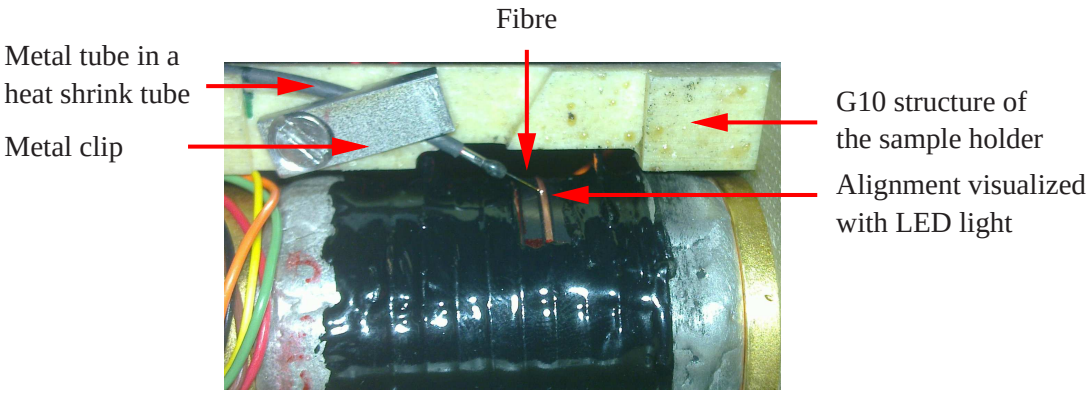

Figure 22. View of the experimental setup. The optical fibre is inside a metal tube which is covered by a heat shrink tube and both are fixed on the G10 structure by a metal clip. The alignment of the light beam is being checked with white LED light which is not harmful for eyes unlike the laser light. The sample in this figure is covered with epoxy to overcome movement issues.

8.2 The experimental setup

The LQT apparatus was installed in a critical current station at CERN [**P3**]. The station consists of a cryostat, which may be cooled down to 4.3 K or 1.9 K and is equipped with a power supply delivering currents up to 2000 A and a superconducting solenoid magnet generating a homogeneous field up to 12 T. The superconducting strand is mounted in a VAMAS barrel which is located in the cryostat at the center of the magnet bore.

The fibre was installed similarly as in the calibration experiment, however outside of the cryostat it was additionally protected with a steel monocoil tube, inside the cryostat partly with a heat shrink tube and at the end with a stainless steel tube. The monocoil tube was required by the safety procedures, the heat shrink tube was installed in order to protect the fragile fibre and the metallic tube was used to guide the end face of the fibre at its target. On top of the metallic tube there was also a heat shrink tube to provide better friction as the tube had to be fixed to the sample holder structure with a metal clip, see figure 22.

The apparatus was successfully used for measuring the minimum quench current curve for a high J_c 0.8 mm RRP superconducting Nb_3Sn strand at 4.3 K [**P3**]. The critical current density was 2951 A/mm^2 at 12 T and 4.3 K and the RRR was 149.

Table 6. Information of the samples used in the study for the perturbation sensitivity of the MTI. The J_c and $B^*_{c_2}$ are measured at 4.3 K.

Sample	RRR	J_c (A/mm^2) @ 12T	$B^*_{c_2}$ (T)	Cu-NonCu
1	129	2674	24.0	1.2
2	21	2790	25.6	1.2

9 Perturbation sensitivity of the MTI

After the concept of the LQT apparatus was proven, it was ready to be used for characterizing the high J_c superconducting strands and most importantly to test the theory of the MTI [**P4**].

Two 0.7 mm RRP 108/127 strands were reacted in a way to have very different RRR with comparable high J_c. They RRR values were 129 and 21, see table 6. After the heat treatment they were prepared for characterization for more details. The conventional V-I and V-H measurements were conducted for sample 1 at 1.9 K and 4.3 K. Directly after the conventional measurements, the LQT was used with different trigger energies (from 0.5 μJ to 23 μJ) to characterize the strand. The LQT is done in a single shot mode: the strand is ramped up to a certain value of current in a constant temperature and applied magnetic field; one pulse of light is sent to trigger the instability. If a quench is detected consequently, it can reasonably be considered as a triggered MTI: the energy sent via laser is by far much smaller the MQE. It should be noted that even if the instability is triggered, quench might not follow if the self-field energy is not sufficiently high. This behavior, *i. e.* partial flux jump, may be seen with an oscilloscope by measuring the voltage over the trigger point, see figure 23.

The laser is set to a constant energy and it is used to find the triggered minimum quench current curve. It is found by repeating the following procedure at the chosen magnetic fields: 1. A selected current is supplied to the strand, 2. the trigger is sent in the strand to quench it, 3. if a quench is detected, the current is reduced and the second phase is repeated. If a quench is not detected, the current is increased and the second phase is repeated unless the current has already been tested. In this case the measurement accuracy is increased. If the accuracy is 10 A or better, the quench current is considered as determined.

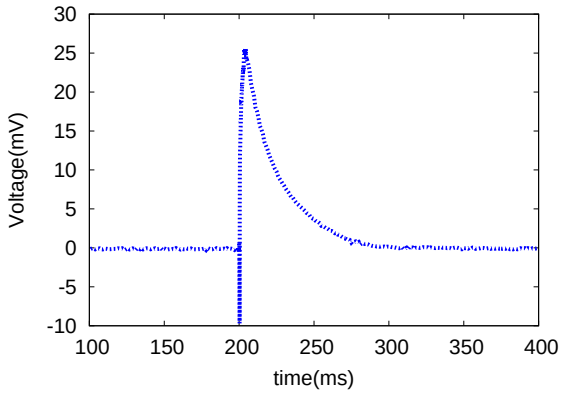

Figure 23. A partial flux jump signal observed with an oscilloscope. The voltage is measured at the LQT trigger point over time when a trigger is given at 200 ms. The signal clearly shows that the instability is triggered since the voltage is built up due to a resistive zone in the strand. However, the signal is reduced to zero again after 50 ms of the triggered instability. The self-field energy together with the trigger energy is not enough to quench the strand.

9.1 Results

The sample 1 corresponds to the one mentioned in subsection 3.4, see figure 8 b for the conventional measurements at 1.9 K. According to the theory it should be possible to trigger a quench in the perturbation dependent region, *i. e.* at fields higher than 8 T, showing that between 8 T and the 13 T-14 T region (being the beginning of the stable zone with respect to MTI) the wire is subject still to MTI but this is not triggered because the energy of natural perturbations is not high enough to trigger it. Indeed, the MTI driven quench is observed with six different trigger energies, see figure 24 a). The minimum quench current line is found with the 23 μJ trigger. It is shown that the perturbation dependent region extends at least until 12 T. Based on graphical extrapolation the stable region starts at about 13.5 T-14 T. Moreover, the other five perturbation energies, or trigger levels, reveal a set of triggerable currents in between the critical surface and the minimum quench current curve as was predicted by the theory (the triggerable current depends on the perturbation energy). Figure 24 b shows the results of sample 1 at 4.3 K with four different trigger energies. The results are similar to the sample 1 at 1.9 K. The PRB is at 3 T and the stable region is above 12 T. Figure 25 shows the α_{MTI} calculated for each corresponding LQT data point in figure 24. It can be seen that $0.92 < \alpha_{\mathrm{MTI}} < 1$, which means that the instability in this measurement range is

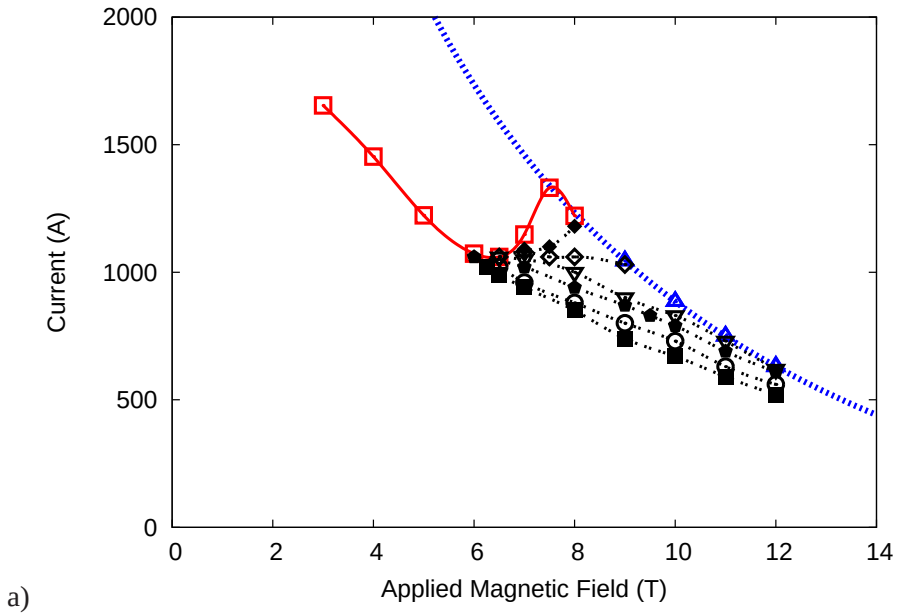

a)

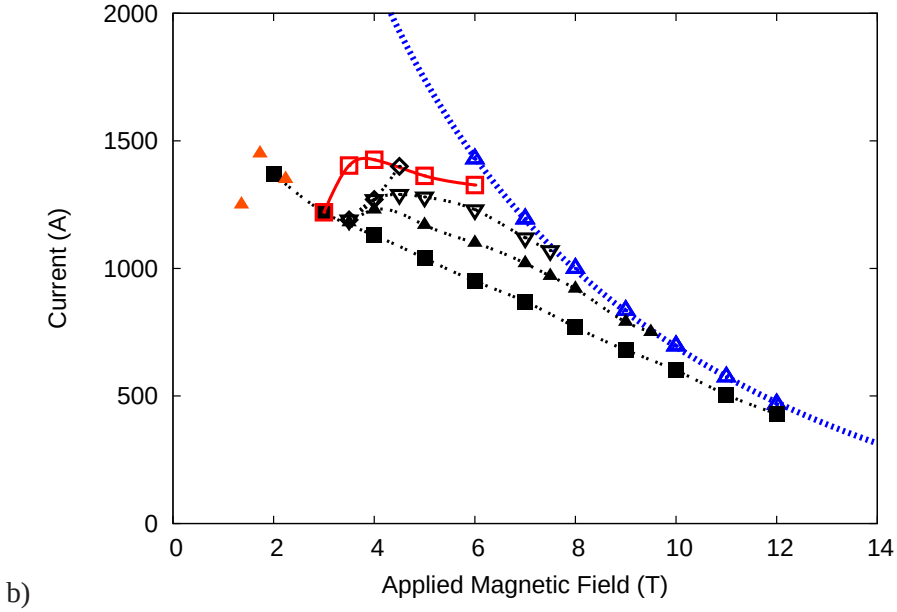

b)

Figure 24. Full characterization of sample 1 with RRR of 129 at a) 1.9 K and b) 4.3 K. (▵) represents the critical current measurements, (····) is the critical surface, (▫) and (▴) represent the quench current by natural perturbation in V-I and V-H, respectively. Laser quenching data is represented by (⬥) 0.5 μJ, (◇) 1 μJ, (▽) 4.4 μJ, (●) 7 μJ, (▲) 10 μJ, (○) 13 μJ, (■) 23 μJ. [**P4**]

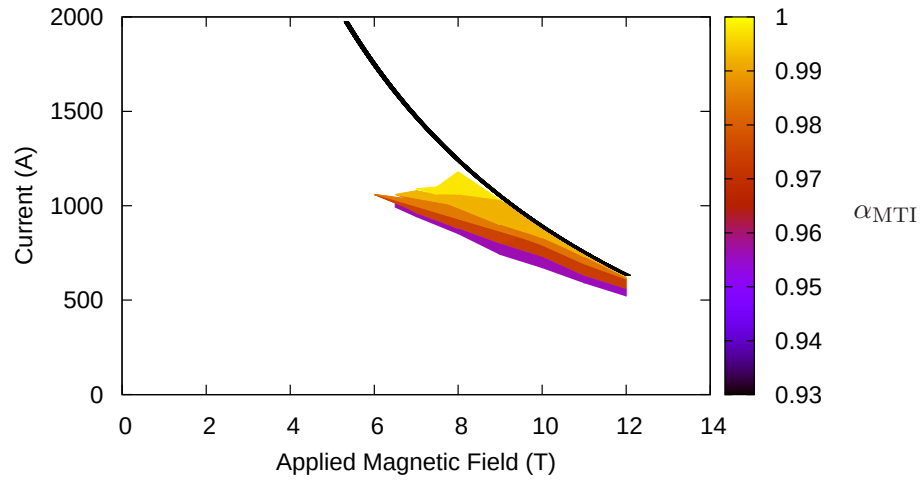

a)

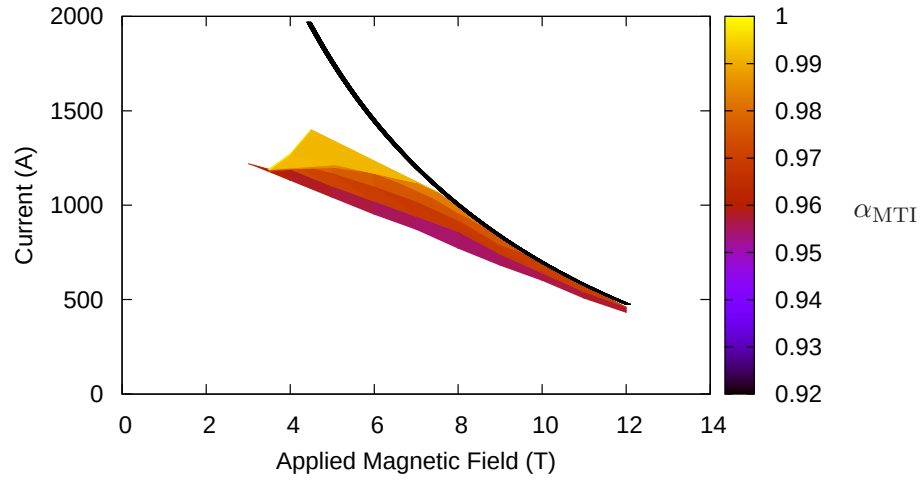

b)

Figure 25. The critical surface and α_{MTI} calculated for the sample 1 with RRR of 129 at a) 1.9 K and b) 4.3 K.

almost purely magneto-thermal. The self-field energy is thus the dominant factor of the instability. The figure shows that the thermal stability becomes more dominant when the magnetic field is increased and the transport current is lowered which is exactly what one would expect. According to the theory, the strand is more unstable when the current density is increased.

According to the theory the magnetization instability can be seen most likely in the low field region [20]. Indeed, at low fields some magnetization instability in V-H measurements is observed, however only at 4.3 K. This has been observed before as well and the lack of quenches at 1.9 K is thought to be due to many small partial flux jumps that dissipate the magnetization energy in small quantities and don't quench the strand [45, 107].

The minimum quench current curves of samples 1 and 2 are compared at 1.9 K and 4.3 K in figure 26. The expected effect of RRR [**P8**] is found: The heat conductivity and the electric conductivity get lower when RRR is decreased. Thus the heat diffusion is slower and the heat generation is more powerful. As a result the quench current is lower throughout the magnetic field range [**P4**].

9.2 The self-field barrier

In [**P4**] the sample 1 was studied in a special way at 1.9 K and 7.5 T with 0.5 μJ trigger energy. First, the sample was quenched to clear the magnetic field distribution. The current was ramped up to 1300 A and then the current was reduced to 1250 A. The trigger was given. The experiment was repeated several times and the sample didn't quench. It is shown in figure 24 a, that normally with 0.5 μJ trigger energy the quench current is at 1100 A. The procedure was improving the stability of the strand, *e. g.* in this case 150 A or more. A new concept called the *Self-Field Barrier* (SFB) is used to explain the behavior and the special way of ramping is called as SFB ramping. At first, in both cases, the current is distributed as described in [13, ch. 7], diffused from outside of the strand towards the center (figure 27 a). However, in SFB ramping the current is over ramped (more current than the target current, figure 27 b) and after the current is decreased, thus again, the current (negative) is diffused from outside towards the center (figure 27 c). The negative current is much less than the positive, and therefore the positive current is at the center and the negative current is around it. The self-field distributions, after the ramp up and after a perturbation, are shown in figure 28 for the normal and SFB ramping. In case of an external perturbation, the negative and positive currents cancel each other, thus redistribution of the transport current might not be necessary. In conventional

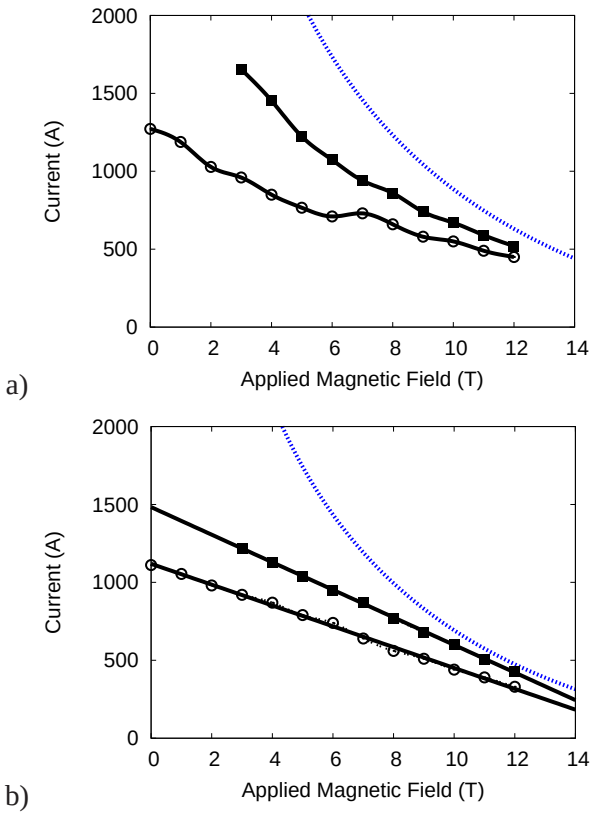

Figure 26. Comparison of the minimum quench current curves between RRR 129 (▪) and 21 (○) at a) 1.9 K and b) 4.3 K. The critical surface is represented by (····).

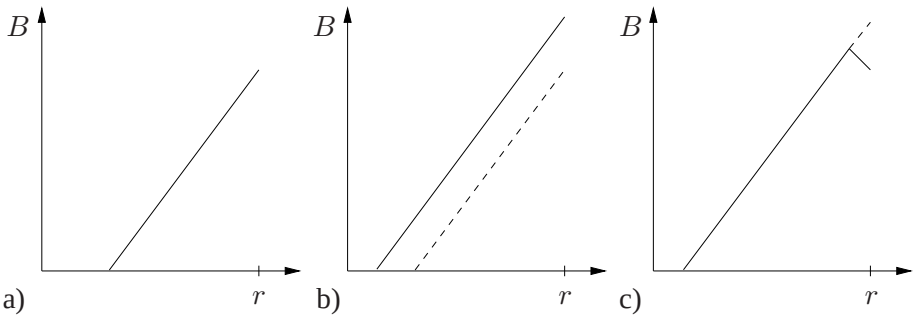

Figure 27. The magnetic field distribution during SFB ramping. There are three phases: a) the ramp up, b) over ramp and c) current decrease. The dashed lines are representing the field distribution in the preceding phase.

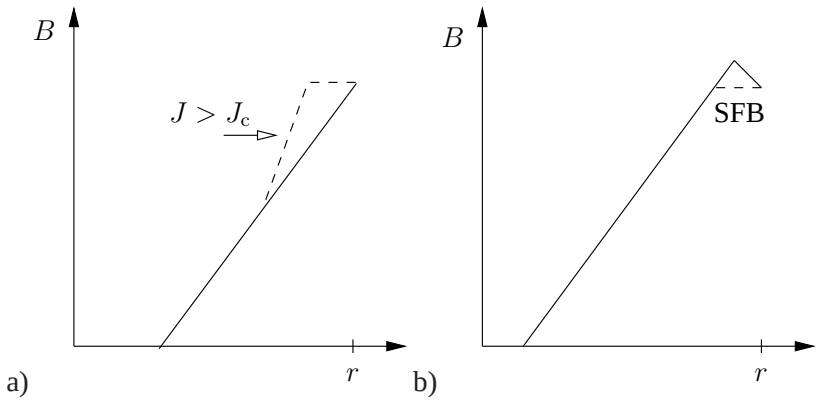

Figure 28. Illustration of the magnetic field distribution in a superconducting slab in case of the a) normal and b) SFB ramp up. The field distribution is represented by continuous and dashed lines before and after the triggering, respectively. It is assumed that the perturbation is high enough to normalize the SFB region.

current distribution, there isn't any negative currents to cancel out the positive one. It may be seen in the figure 28 that the self-field distribution in SFB ramping reduces the necessity of current redistribution in case of a perturbation. The SFB ramping may be generalized [**P4**] so that the SFB field distribution is completely flat. Thus, the general SFB is a stable region in the superconductor between the transport current and the perturbation, see figure 29. Of course it is possible to generate such a strong perturbation which is thermally penetrating the SFB, however more energy is needed.

In the first order of SFB ramping (figure 27) the SFB contains one pair of opposite magnetization currents and in the second order two pairs. Thus by increasing the order, the magnetization can be reduced until the magnetization currents reach the elementary units of magnetization, *i. e.* the Abrikosov's flux line lattice. In superconducting material, it is impossible that the magnetization currents vanish since the material reacts to the self-field of the transport current. However, by increasing the SFB order, one can reduce the level of magnetization and thus increase the stability of the SFB.

In simple terms, in first approximation the flux line lattice can be neglected and thus the SFB is analogical to a barrier of normal material between the external perturbation and the transport current. The thermal shock generated by the perturbation can be partly absorbed by the barrier material. Thus, the enhanced stability is even more evident. One should note that there is still a conceptual difference between the SFB and a barrier made of normal material. The SFB requires well defined procedures in order to generate it while the normal material barrier would not. Moreover the SFB will always contain

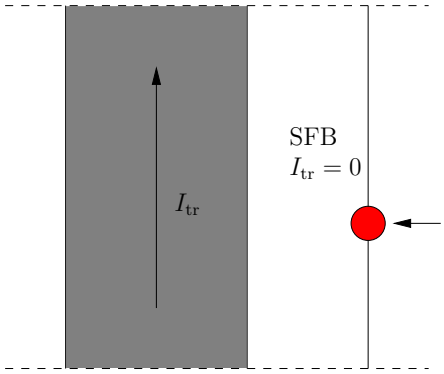

Figure 29. Illustration of the general SFB in a superconducting slab. The current is forced to flow on the left hand side leaving a zone without transport current (SFB) in between the right surface of the slab and the zone that contains all the transport current. The red dot represents an external perturbation. One can see that the perturbation does not directly effect on the transport current, which makes the configuration more stable compared to a situation where the transport current flows right next to the perturbation event.

at least the flux line lattice which a normal material barrier would not.

It is unclear how well the SFB could be applied into superconducting magnets. Would it actually help to enhance the stability in an environment where the natural perturbation is high? At the moment the question remains unanswered. However, the SFB is extremely interesting new concept and scientific tools for investigating it are developed. Thus in the future, the SFB should be one phenomenon to be studied in order to assess the practical benefits of it.

9.3 The role of trapped flux

One should note that the SFB may be generated only into a superconductor that has strong pinning: the magnetic flux is trapped inside the superconductor which makes it possible to manipulate the magnetic field distribution. The importance of the flux trapping with regard to the stability in bulk superconductors is studied in [108]. The authors describe the benefits of the phenomenon: the existing magnetic field distribution in a superconductor does not contribute to the electric field and thus the magnetic field distribution is the sum of the initial and induced distributions (even if the temperature is varied). They state that for this reason the stability conditions are dependent of the state of the trapped flux. To highlight this important work, one should note that in [109,

p. 74] the author proposes an experiment of a *thermal way (chemin termique)* to induce a stable magnetization in a superconducting slab (even if the slab would conventionally be unstable).

The thermal way is such that the magnetic field is increased (from 0 T to 8 T) while the superconductor is cooled down (from 9.3 K to 4.3 K). Thus at higher temperatures the induced screening current can penetrate deeper into the conductor than it would at 4.3 K, because $J_{\mathrm{c}}(T) < J_{\mathrm{c}}(4.3\ \mathrm{K})$ when $T > 4.3$ K. Moreover, the current tends to stay in place even when the temperature is decreased due to the trapped flux [108]. The magnetic field distribution is now more stable than if the temperature would have been at 4.3 K to begin with. The increased stability is due to the magnetic field distributions at higher temperatures, which are more stable than the conventional distribution at the final temperature (4.3 K).

Similar idea to the thermal way was also applied to a quadrupole magnet in [**P6**]. The magnet was ramped up to 12.2 kA at 4 K and after that the temperature was decreased to 1.9 K without inducing a quench. In a conventional measurement the magnet quenched above 11.6 kA. Thus, the quench current was improved by more than 600 A. This slightly different procedure to the thermal way was named as the *cooldown experiment*.

The cooldown experiment is not a solution for achieving better stability for a magnet. This was realized in [**P6**] when the magnet quenched some hours after the stable state was achieved. The reason is that in a superconducting strand, the inner filaments are further away from the surface of the strand in terms of electrical resistance, because in between the filaments there is the copper matrix that has some resistivity: the path (in normal metal) from the surface of the strand to the inner filaments is longer than to the outer ones. Therefore, as the current enters into the strand from the side, eventually the outermost filaments are the preferable route for the current. However, it will take some time for the current to redistribute to the ultimate route due to *inductive effects* (will be explained later). Therefore, even if the current would be forced to flow in the innermost filaments by using the thermal way, it would eventually prefer the outermost filaments. Thus, the more stable state after the thermal way would degrade over time which explains the fact that eventually the magnet quenched in the cooldown experiment. This issue was understood by Bordini, who proposed the experiment in [**P5**] that will be discussed in the next section. Actually, this experiment and its results lead to the discovery of the SFB enhanced stability.

10 Filament cut technique

The SFB can enhance self-field stability in superconducting strands because it reduces the transport current at the outermost sub-element layer, however it is not guaranteed that the SFB lasts for infinite amount of time, *e. g.* after a flux jump. When a certain technique is used, the strand can be ramped up with a normal ramp up scheme, and still the SFB is induced. In this case the SFB lasts. This technique is called the *filament cut technique* [**P5**]. In the conventional strand, without the cutting, the current would always flow in the outermost sub-elements due to the *inductive* and *resistive* effects. The outermost sub-elements have the lowest inductance and therefore the current prefers to flow in them when the current is ramped up (inductive). Moreover, the current enters to the strand from the side and thus there is no reason to flow to the innermost sub-elements unless the outer ones are full (resistive). It is possible to cut one or two sub-element layers in the splice region in order to change the resistive effect and thus force the current in the innermost sub-elements. It is notable that even if the sub-elements are cut, it doesn't reduce the nominal current carrying capacity since the cut is made in the splice region, where the current enters to (or exiting from) the strand. Figure 30 shows an axisymmetric representation of the three layer strand with cuts. The geometry is used in an electromagnetic FEM model [**P5**] for finding the current density distribution. The cuts are made by grinding the surface of the strand. An example of the cutting is shown in figure 31. The grinding takes advantage of the twisting of the sub-elements. The length of the cut needs to be longer than the twist pitch to make sure that all of the sub-elements in the cut layer are discontinuous. By using the filament cut technique, the current carrying capacity is intact and the current has a possibility to flow in the innermost sub-elements even if the outer ones are not full, thus creating an SFB at the outermost sub-element. While in the conventional situation the current always flows in the outermost sub-elements [13, ch. 7].

The axisymmetric FEM model (figure 30) shows that the current can flow through the innermost sub-elements even if the first layer is not full. In order to understand this better, for simplicity, the system may be thought of as an electric circuit shown in figure 32. The L_1, L_2 and L_3 represent the inductances of the superconducting sub-element layers. The sum of the resistors $R_i + R_\mathrm{s}$ represent the path from the splice to the i^th sub-element layer, where $i \in \{1, 2, 3\}$. The R_s is a residual resistance between the splice and the first layer. If there are no cuts and the first layer is not full, the R_1 can be set to zero and all the current thus flows through the first layer. If the cuts are present, all of the resistances exist and thus the current flows in all of the layers. However, it

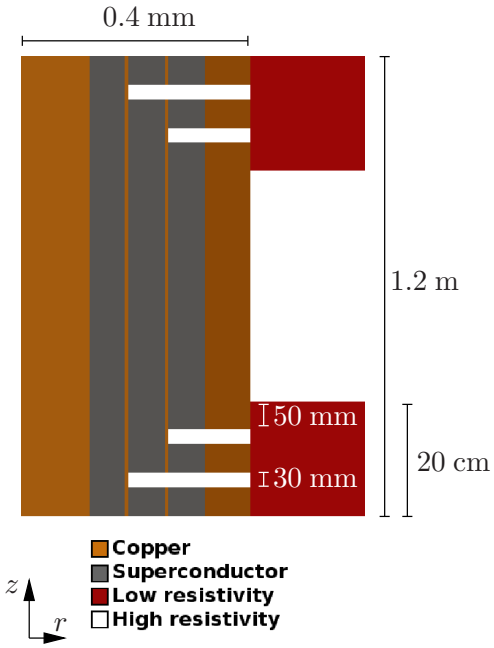

Figure 30. Axisymmetric geometry for a 3-layer strand, where the symmetry axis is located on the left hand side. The model is for finding the current density distribution. The transport current is applied to and out of the model through the low resistivity blocks. It is to ensure equipotential boundaries for the splice. The cut is modeled as a discontinuity in the superconducting sub-element layer filled with highly resistive material. The length of all of the cuts is 30 mm and 50 mm is left for the current to enter to the first layer. It should be noted that this sketch is not to scale: in reality the radial length of the model is 0.4 mm while the height is 1.2 m.

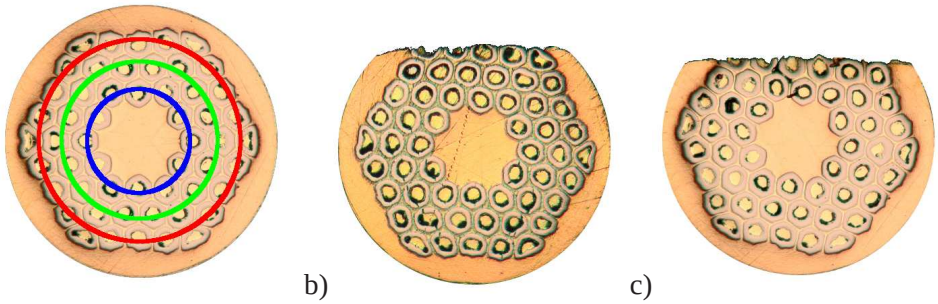

Figure 31. Optical microscope view of the 0.8 mm RRP 54/61 strand cross-section after the sub-element cut preparation. a) Intact strand, where the red, green and blue circles represent the first, second and third sub-element layers, respectively, which are used in the axisymmetric presentation; b) strand whose first layer is cut and c) strand whose first and second layers are cut.

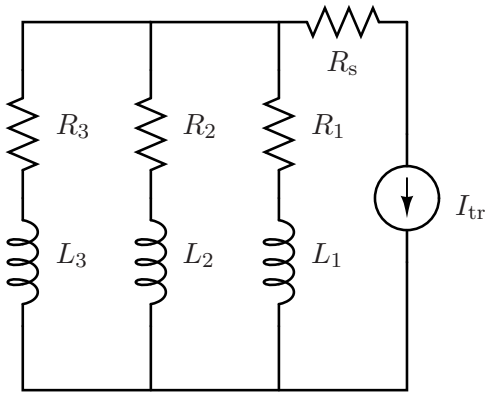

Figure 32. A cut prepared strand with three sub-element layers represented by an electric circuit.

is notable that the inductance is higher in the innermost sub-elements [13, ch. 7] and therefore if the current is ramped up very quickly the current first prefers to flow in the outermost sub-element layer and thus making the situation similar to the conventional current distribution. However, when the time elapses and system approaches steady state the inductive effect fades away, thus the resistances define the final current distribution. Figure 33 shows an example calculation with the axisymmetric model. When the current is the ramped up, most of the transport current stays in the first sub-element layer. However, when the ramp stops the transport current is reduced in the outermost layer while the current in both of the innermost layers is increased. Such a behavior is not seen without the cut, the current stays in the first sub-element layer. The model confirms the behavior which is described by the electric circuit model. An example of the final state of the SFB generation in the cut sample calculated with the FEM model is shown in figure 34. The magnetization that is induced in the outermost and the middle layers is due to self-field of the transport current. When the sub-elements are cut, the transport current is forced to flow in the innermost layer, thus self-field is created which induces a magnetization current in the outermost layers. While if the cut is missing, all the transport current flows in the outermost layer. This fact is supported by the final state calculated with the axisymmetric model.

Figure 35 shows the critical and stability measurement results [**P5**] of a 0.8 mm RRP 54/61 strand with cut preparation and as a reference, similar *witness* sample without cutting, see table 7 for more details. Witness sample means that the sample is prepared similarly and at the same time as the sample of interest. At first, the V-I measure-

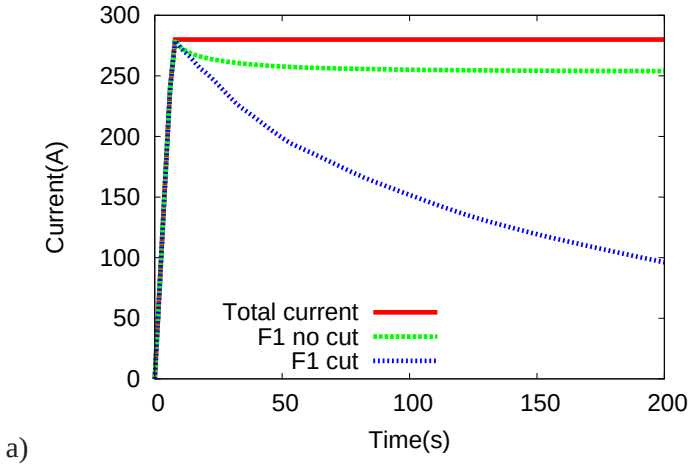

a)

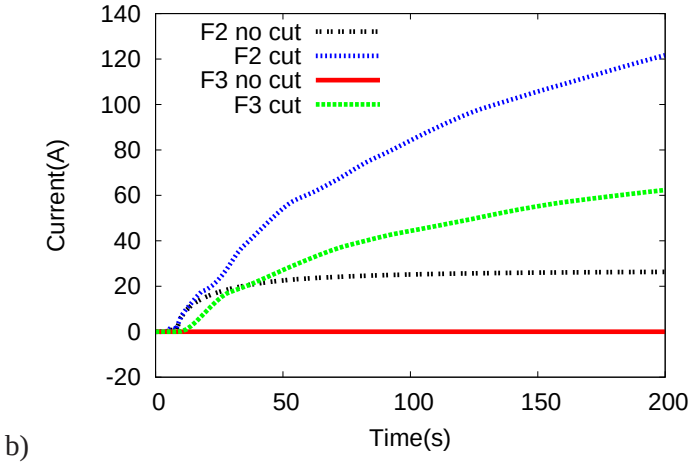

b)

Figure 33. A current evolution in sub-element layers according to the axisymmetric strand model. The sub-element layers are named F1, F2 and F3; F1 being the outer sub-element layer. The current is ramped up to 280 A in 10 seconds and then kept constant. The figures are showing the principle, they are not to be compared with the experimental results.

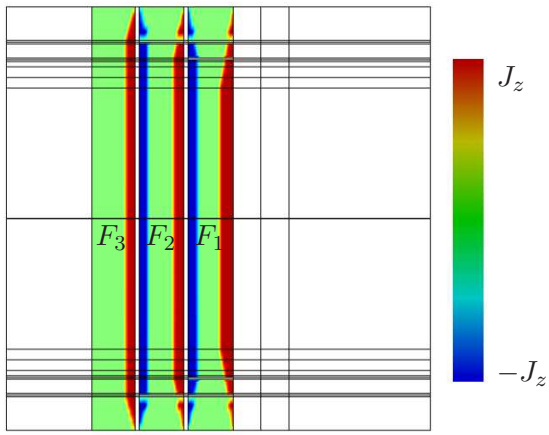

Figure 34. The final state of the z-component (up/down) of the current density distribution in the RRP 0.8 mm strand showing the generated SFB. The geometry of the picture corresponds to the geometry presented in figure 30. There are clearly SFBs in the outermost F_1 and the middle F_2 sub-element layers. Negative current in the center side and positive current in the outer side of the outermost sub-element. Moreover, the level of transport current is minimal.

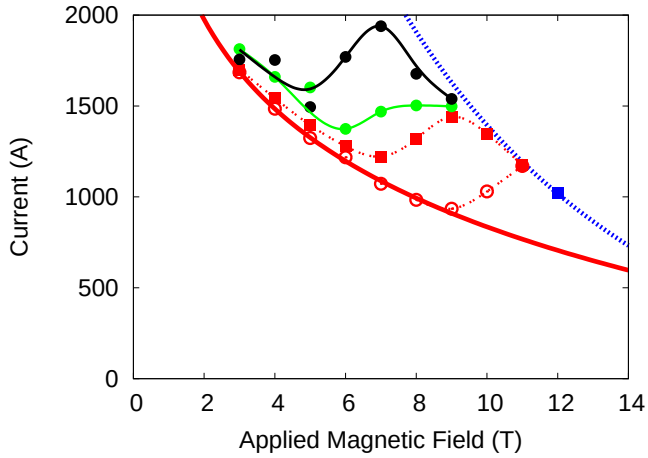

Figure 35. I_c- and stability measurements. (····) is I_c surface, (⊙) is witness sample quench current curve, and (—) is logarithmic fit for (⊙). (▪) is quench current for cut sample with 20 A/s ramp rate, (•) is quench current with 20 A/s ramp rate which includes 100 s waiting below the quench current of (▪), (•) is quench current with 1 A/s ramp rate. Excluding the minimum quench current curve fit (—), the lines are drawn in order to facilitate viewing, they are not fit functions.

Table 7. $B^*_{c_2}$ and J_c at 4.3 K, 12 T.

	I_c(A)	J_c(A/mm^2)	$B^*_{c_2}$(T)
Cut	768	3056	25.2
Witness	771	3069	25.3

ments of the witness sample were conducted (⊙). Premature quenching was observed below 12 T. The behavior can be explained by the theory of the self-field instability [45]. The V-I measurements of cut sample were done with 20 A/s (▪), 20 A/s including a 100 s plateau in current below the minimum quench current determined with the preceding measurement (•) and with 1 A/s ramp rate (•). Clear improvement with respect to the witness sample is observed. The first measurements with a ramp rate of 20 A/s show that the PRB is at 9 T for the witness sample and 6 T for the cut sample. It seems that the cut sample is more stable. It has been already explained in subsection 3.4 that the natural perturbation can vary among the different measurements, which could explain the difference. However, the PRB is moved to 5 T when the 100 s pause is kept just below the minimum quench current measured with 20 A/s. The PRB is further decreased to 4 T with a ramp rate of 1 A/s and the difference between the 20 A/s measurement in quench current at 7 T is almost 900 A. The results can be explained by the SFB enhanced stability and the ramp rate dependency of the system that was described above. First, the current flows at the outermost sub-elements, providing stability comparable to the witness sample. When a 100 s pause is kept, the current has time to diffuse in the innermost sub-elements generating the SFB type distribution to the outer sub-element, which increases the stability of the cut strand. When the ramp rate of 1 A/s is used the current has even more time to generate the SFB and thus the stability is further increased. For fast ramp rate the inductive effect dominates and the current will flow only in the outermost sub-elements. Thus the lower is the ramp rate, the larger is the beneficial effect of the filament cut technique on the strand stability. Since in accelerator magnets the ramp rate is very low, expecially in colliders like LHC, this technique could be applied to practical magnets, if a suitable and safe technology for manipulating strand in a cable is found. Moreover, the filament cut technique shows the correctness of the SFB (self-field barrier), since it is based on the same idea of ”forcing” the transport current to be carried by the innermost sub-elements, rather than by the outermost as it would naturally happen.

11 Conclusion

The LHC upgrade projects require high performance superconducting strands, which may be severely limited by the MTI. The perturbation sensitivity suggested by the theoretical and experimental results has not been put into a rigorous test until now.

Remarkable leap in the development of the energy deposition systems was taken when the LQT system was first introduced [72], where the main focus was to study the thermal stability of NbTi strands which does not require such a short pulse widths as in this work. The LQT system was further developed and tested in this thesis and it is so far the only system which can be used for studying the MTI. Compared to the LQT, the older systems are too slow or they suffer from fundamental energy efficiency problems. The LQT system is optimized for depositing energy in the strand for highest possible efficiency. In [72] it was done by blackening the strand surface in order to maximize the optical absorptivity when IR-wavelengths were used. In this thesis the absorptivity is optimized with respect to wavelength. *A priori*, the highest absorption would be at the plasma frequency, which is not withstood by the all-silica fibre, the chosen wave guide. Thus, it is necessary to choose the lowest possible wavelength suitable for the fibre.

Shortest wavelength which can be transmitted by the unloaded fibre without inducing irradiation damage is 330 nm. The fibre can withstand shorter wavelengths if it is loaded with hydrogen, however it is not a practical solution since the fibre needs to be below -18°C all the time so that the hydrogen stays inside the fibre.

Q-switching is a natural way of generating an energetic and short pulse of laser light which is needed for studying the perturbation sensitivity of the MTI. The diode pumped Nd-YAG crystal at 1064 nm is a common choice for the active medium. In this work it is chosen as the light source with second and third harmonics providing 532 nm and 355 nm wavelengths. The 355 nm is just above the irradiation damage low limit for the unloaded all-silica fibre. The calibration of the LQT is a modified version of [72] which was relaying to the Wiedemann-Frantz law. The calibration in this work is done against a known heater in a vacuum chamber at 4.2 K. The calibration shows that the optical absorptivity of copper at 355 nm and 532 nm are 83% and 89%, respectively, which are much higher than the values 60% and 40% in literature. This difference is due to different surface properties or the high pulse energy which is reported to increase the absorptivity. The corresponding cryogenic losses in the fibre are 5.5% and 1.8%.

For the first time, the existence of the minimum quench current curve with respect to MTI is confirmed at 1.9 K and 4.3 K by using the LQT apparatus. Below the curve, MTI cannot quench the strand. The tested strand is the 0.7 mm RRP 108/127 with

RRR of 129 which is the conductor of interest in the upgrade projects of the LHC. The (weak) RRR dependence was verified by measuring a low RRR wire with similar critical current. The LQT is also used to reveal sets of triggerable currents that are in the perturbation dependent region. Clearly, the experimental data shows that the perturbation independent, dependent and stable regions are found as predicted by the theory. The α_{MTI} is calculated from the corresponding LQT triggered currents yielding values between 0.92 and 1 which means that the instability is almost purely magneto-thermal. It should be noted that it is possible to quench the strand below the minimum quench current curve, however the α_{MTI} decreases which means that the instability becomes thermal.

The LQT apparatus is used to prove that the newly introduced self-field instability related concept, SFB, enhances the stability of a strand. The SFB contains opposite currents that can cancel each other. Therefore current redistribution does not occur in this region in case of an external perturbation. When such a region is put between the surface of a superconductor and the transport current, the region can act as a stable barrier which can absorb the thermal shock. Thus the SFB is a thermal barrier between the perturbation point and the transport current. In a first approximation, where the magnetization currents and the Abrikosov's flux line lattice are neglected, it is analogical to a barrier made of normal material.

The SFB can be induced at least in two different ways which are presented in the thesis: 1. the SFB ramping where, in the first order, the current is increased more than the target current and then reduced to the target current or 2. via the filament cut technique where the current is forced to the innermost filaments of the strand. The SFB ramping is not recommended for the magnets because the SFB currents are not fully persistent. Actually a way to circumvent could be a useful further investigation. The cut filament technique is in principle applicable to magnets, however the inductive effect might restrict heavily the ramp rates since the current prefers the outermost filaments due to the lower inductance leading to reduced stability. On the other hand, if the slow ramp rate is not a problem the technique could be applicaple also in practice. It should also be noted that cutting some filament in a strand of a real magnet is a dangerous solution that probably would never be accepted as a working method. However the experiment on the cut filament sample has unequivocally demonstrated the possibility of using the SFB concept.

References

[1] L. Evans, *The Large Hadron Collider: a Marvel of Technology* (CERN and EPFL Press, 2009).

[2] L. Rossi, Cryogenics **43**, 281 (2003).

[3] CERN inauguration, 2008, https://lhc2008.web.cern.ch/lhc2008/inauguration/lhcexpo.html.

[4] LHC Design Report, CERN, EDMS 445839.

[5] M. Lamont, THE LHC FROM COMMISSIONING TO OPERATION, *in Proceedings of IPAC2011*, (2011).

[6] LHC Design Report I, CERN, EDMS 445831.

[7] L. Bottura, G. de Rijk, L. Rossi and E. Todesco, MT22 Conference paper (2011).

[8] L. Rossi, LHC UPGRADE PLANS: OPTIONS AND STRATEGY, *in Proceedings of IPAC2011*, (2011).

[9] L. Rossi and R. D. Maria, SUMMARY SESSION 08: HIGH LUMINOSITY (HL-LHC), *in Proceedings of Chamonix 2011 workshop on LHC Performance*, (2011).

[10] L. Rossi, Supercond. Sci. Technol. **23**, 034001 (17pp) (2010).

[11] M. Bajko *et al.*, REPORT OF THE TASK FORCE ON THE INCIDENT OF 19 SEPTEMBER 2008 AT THE LHC, CERN, LHC Project report 1168.

[12] INTERIM SUMMARY REPORT ON THE ANALYSIS OF THE 19 SEPTEMBER 2008 INCIDENT AT THE LHC, CERN, EDMS 973073.

[13] M. N. Wilson, in *Superconducting Magnets* (Oxford university press, 1983).

[14] E. Barzi *et al.*, IEEE Trans. Appl. Supercond. **15**, 3364 (2005).

[15] A. K. Ghosh, L. D. Cooley and A. R. Moodenbaugh, IEEE Trans. Appl. Supercond. **15**, 3360 (2005).

[16] D. R. Dietderich *et al.*, IEEE Trans. Appl. Supercond. **15**, 1524 (2005).

[17] A. K. Ghosh, E. Gregory and X. Peng, IEEE Trans. Appl. Supercond. **21**, 2380 (2011).

[18] G. Ambrosio *et al.*, IEEE Trans. Appl. Supercond. **20**, 283 (2010).

[19] Superconducting Applications Group, J. Phys. D: Appl. Phys **3**, 1517 (1970).

[20] V. V. Kashikhin and A. V. Zlobin, IEEE Trans. Appl. Supercond. **15**, 1621 (2005).

[21] R. G. Mints and A. L. Rakhmanov, Sov. Tech. Phys. Lett. **2**, 193 (1976).

[22] B. Bordini and L. Rossi, IEEE Trans. Appl. Supercond. **19**, 2470 (2009).

[23] S. Brandt, *The Harvest of a Century: Discoveries in Modern Physics in 100 Episodes* (OUP Oxford, 2008).

[24] C. Enss and S. Hunklinger, *Low-Temperature Physics* (Springer, 2005).

[25] C. P. Poole, H. A. Farach, R. J. Creswick and R. Prozorov, *Superconductivity* (Academic Press, 2004).

[26] J. Bardeen, L. Cooper and J. R. Schrieffer, Physical Review **108**, 1175 (1957).

[27] S. Fujita, K. Ito and S. Godoy, *Quantum Theory of Conducting Matter* (Springer, 2009).

[28] L. P. Gor'kov, Soviet Physics JETP **36(9)**, 1364 (1959).

[29] F. London and H. London, in *Proc. Roy. Soc.*, *A149* (London, 1935), pp. 71–88.

[30] C. P. Poole, *Handbook of Superconductivity* (Academic Press, 2000).

[31] A. A. Abrikosov, Soviet Physics JETP **5**, 1174 (1957).

[32] A. V. Gurevich, R. G. Mints and A. L. Rakhmanov, *The Physics of Composite Superconductors* (Begell House, 1997).

[33] M. Peurla, Ph.D. thesis, University of Turku, 2007.

[34] R. G. Mints and A. L. Rakhmanov, J. Phys. D **8**, 1769 (1975).

[35] C. P. Bean, Physical review letters **8**, 250 (1962).

[36] C. P. Bean, Reviews of Modern Physics **36**, 31 (1964).

[37] Y. B. Kim, C. F. Hempstead and A. R. Strnad, Physical Review **129**, 528 (1963).

[38] P. F. Smith and P. Colyer, Cryogenics **5**, 201 (1975).

[39] H. Brechna, *Superconducting Magnet Systems* (Berlin: Springer, 1973).

[40] E. Barzi, P. J. Limon, R. Yamada and A. V. Zlobin, IEEE Trans. Appl. Supercond. **11**, 3595 (2001).

[41] R. Hancox, IEEE Trans. Magn. **MAG-4**, 486 (1968).

[42] M. G. Kremlev, Cryogenics **14**, 132 (1973).

[43] C. P. Bean and J. D. Livingstone, Phys. Rev. Lett. **12**, 14 (1964).

[44] B. Bordini, Ph.D. thesis, Fermilab, 2006.

[45] B. Bordini *et al.*, IEEE Trans. Appl. Supercond. **18**, 1309 (2008).

[46] B. Bordini, personal communication, 2012.

[47] G. Willering, Ph.D. thesis, University of Twente, 2009.

[48] A. Devred, J. Appl. Phys. **67**, 7467 (1989).

[49] E. S. P. Bauer, H. Rajainmaki, Technical report, EDFA, Max-Planck-Inistitute fur Plasmaphysik (unpublished).

[50] L. Bottura and B. Bordini, IEEE trans. appl. supercond **19**, 1521 (2009).

[51] C. N. Carter, K. G. Lewis and B. J. Maddock, Cryogenics **13**, 337 (1973).

[52] M. N. Wilson, IEEE Trans. Magn. **MAG-13**, 440 (1977).

[53] M. N. Wilson, IEEE Trans. Magn. **MAG-17**, 1815 (1981).

[54] M. N. Wilson and Y. Iwasa, Cryogenics **18**, 17 (1978).

[55] M. J. Superczynski, IEEE Trans. Magn. **MAG-15**, 325 (1979).

[56] C. Schmidt, Cryogenics **27**, 605 (1978).

[57] J. Duchateau and B. Turck, J. Appl. Phys **46**, 4989 (1975).

[58] D. E. Baynham, V. W. Edwards and M. N. Wilson, IEEE Trans. Magn. **MAG-17**, 732 (1981).

[59] C. A. Scott, Cryogenics **22**, 577 (1982).

[60] D. Baynham, D. Cragg and R. Coombs, IEEE Trans. Appl. Supercond. **9**, 1109 (1999).

[61] K. Seo *et al.*, IEEE Trans. Magn. **32**, 3089 (1996).

[62] S. W. Kim *et al.*, IEEE Trans. Magn. **32**, 2784 (1996).

[63] A. K. Ghosh, W. B. Sampson and M. N. Wilson, IEEE Trans. Appl. Supercond. **7**, 954 (1997).

[64] A. Ghosh *et al.*, Physica C **310**, 335 (1998).

[65] A. P. A.K. Ghosh *et al.*, IEEE Trans. Appl. Supercond **9**, 251 (1999).

[66] N. Amemiya *et al.*, Cryogenics **43**, 249 (2003).

[67] P. Bauer, J. Donnier and L. R. Oberli, IEEE Trans. Appl. Supercond **9**, 1141 (1999).

[68] New FRESCA sample holder for cable stability experiments, Technical Report, CERN - AT/MCS internal note 2005-11, EDMS 691690, 2005.

[69] F. Trillaud *et al.*, IEEE Trans. Appl. Supercond **15**, 3648 (2005).

[70] M. W. de Rapper, Ph.D. thesis, University of Twente, 2012.

[71] F. Trillaud *et al.*, Cryogenics **45**, 585 (2005).

[72] F. Trillaud, Ph.D. thesis, Inistitut nationale polytechnique de Grenoble, 2005.

[73] K. Yamada, M. Aoki and Y. Matsui, Cryogenics **48**, 518 (2008).

[74] H. P. Myers, *Introductory Solid State Physics* (Taylor & Francis, 1997).

[75] E. E. Koch, C. Krafka, D. W. Lynch and J. H. Weaver, *Optical properties of metals* (Eggenstein-Leopoldshafen : Karlsruhe Fachinformationszent. Kernforsch. Zentralstelle At. Energ., 1981).

[76] M. A. Biondi and A. I. Guobadia, Physical review **166**, 667673 (1968).

[77] B. Saleh and M. Teich, *Photonics* (Wiley, 2007).

[78] J. M. Senior, *Handbook Of Optics* (Prentice/Hall International, 1985), Vol. Principles And Practice.

[79] K. Zhang and D. Li, *Electromagnetic Theory for Microwaves and Optoelectronics*, 2nd ed. (Springer, 2007).

[80] M. R. Spiegel and J. Liu, *MATHEMATICAL HANDBOOK OF FORMULAS AND TABLES*, 2nd ed. (Magraw-Hill, 1999).

[81] M. Bass, E. W. V. Stryland, D. R. Williams and W. L. Wolfe, *Handbook Of Optics*, 2nd ed. (McGraw-Hill, 1995), Vol. II.

[82] T. G. Brown *et al.*, *The Optics Encyclopedia* (Wiley-VCH, 2004), Vol. 1.

[83] C. F. Bohren and D. R. Huffman, *Absorption and scattering of light by small particles* (Wiley-VCH, 2010).

[84] J. Crisp and B. Elliott, *Introduction to Fiber Optics* (Newnes, 2005).

[85] M. Skorobogatiy, K. Saitoh and M. Koshiba, Optics Express **16**, 14945 (2008).

[86] M. Bass, E. W. V. Stryland, D. R. Williams and W. L. Wolfe, *Handbook Of Optics*, 2nd ed. (McGraw-Hill, 1995), Vol. I.

[87] J. W. Fleming and D. L. Wood, App. opt. **22**, 3102 (1983).

[88] C. M. Smith and L. A. Moore, Journ. of Fluor. Chem. **122**, 81 (2003).

[89] M. Oto *et al.*, Journ. of noncryst. sol. **349**, 133 (2004).

[90] D. L. Griscom, Journ. of Non-cryst. sol. **73**, 51 (1985).

[91] D. L. Griscom, Journ. of Non-cryst. sol. **68**, 301 (1984).

[92] V. Kh.Khalilov *et al.*, SPIE-Proc. **6083**, 48 (2006).

[93] T. Mizunamia and K. Takagia, Opt. comm. **68**, 223 (1988).

[94] R. S. Taylor, K. E. Leopold, R. K. Brimacombe and S. Mihailov, App. opt. **27**, 3124 (1988).

[95] R. S. Taylor, K. E. Leopold, R. K. Brimacombe and S. Mihailov, Appl. Opt. **27**, 3124 (1988).

[96] K.-F.Klein *et al.*, Sensors and Actuators **B38-39**, 305 (1997).

[97] P.Karlitschek, G.Hillrichs and K.-F.Klein, Opt. Comm. **155**, 376 (1998).

[98] J. Assmus *et al.*, Int. Conf. on Ageing Studies and Lifetime extension of materials **paper 6.2**, (1999).

[99] K.-F.Klein *et al.*, SPIE-Proc. BiOS'98 **3262C**, 150 (1998).

[100] K.-F. Klein *et al.*, SPIE-Proc. BiOS'01 **4253**, 42 (2001).

[101] W.Koechner, *Solid-State Laser Engineering*, 6^{th} ed. (Springer, 2006).

[102] J. Geusic, H. M. Marcos and L. V. Uitert, Appl. Phys. Lett. **4**, 182 (1964).

[103] P. Technologies, Data sheet for Silica/Silica optical FV fibres, World Wide Web electronic datasheet, http://www.datasheet.org.uk/FVP100110125-datasheet.html, 1998.

[104] L. Tunna, A. Kearns, W. O'Neill and C. J. Sutcliffe, Opt. Las. Tech. **33**, 135 (2001).

[105] B. Karlsson and C. G. Ribbing, J. Appl. Phys. **53**, 6340 (1982).

[106] A. Y. Vorobyev and C. Guo, Journ. Appl. Phys. **110**, 043102 (2011).

[107] B. Bordini, To be presented at ASC 2012.

[108] J. L. Noel, A. Mailfert and G. Fournet, Le journal de physique **32**, 191 (1971).

[109] A. Mailfert, Ph.D. thesis, Université de Paris, 1969.